



NRL/MR/6040--12-9426

## Development of a Four-Fin Bio-Inspired UUV: CFD Studies

RAVI RAMAMURTI

JASON GEDER

*Laboratory for Propulsion, Energetic, and Dynamic Systems  
Laboratories for Computational Physics and Fluid Dynamics*

September 4, 2012





## Table of Contents

<b>INTRODUCTION .....</b>	<b>1</b>
<b>THE INCOMPRESSIBLE FLOW SOLVER .....</b>	<b>2</b>
<b>RESULTS AND DISCUSSION .....</b>	<b>2</b>
<b>VEHICLE SELECTION: .....</b>	<b>2</b>
<i>Effect of angle of attack: .....</i>	<i>5</i>
<i>Effect of Side Slip angle: .....</i>	<i>6</i>
<i>Turn rate characteristics: .....</i>	<i>6</i>
<i>Effect of axial separation of the fins: .....</i>	<i>7</i>
<b>PARAMETRIC STUDIES: .....</b>	<b>9</b>
<i>Effect of Phasing of the Rear Fin: .....</i>	<i>10</i>
<i>Effect of Vehicle Speed: .....</i>	<i>15</i>
<i>Vertical Position Control: .....</i>	<i>19</i>
<i>Yaw Maneuver: .....</i>	<i>23</i>
<i>Effect of Fin Orientation: .....</i>	<i>27</i>
<i>Yaw Maneuver using Symmetric Fin Orientation: .....</i>	<i>29</i>
<i>Dive Maneuver using Symmetric Fin Configuration: .....</i>	<i>30</i>
<i>SUMMARY .....</i>	<i>31</i>
<b>ACKNOWLEDGEMENTS .....</b>	<b>32</b>
<b>REFERENCES .....</b>	<b>32</b>

## List of Figures

Fig. 1. Flow past a rectangular cross section vehicle.....	3
Fig. 2. Flow past a modified rectangular cross section vehicle. ....	3
Fig. 3. Flow past a modified rectangular cross section vehicle without mounting caps.....	4
Fig. 4. Flow past a modified rectangular cross section vehicle with side slots. ....	4
Fig. 5. Flow past a vehicle with elliptical cross section. ....	4
Fig. 6. Flow past a vehicle with elliptical cross section with fins. ....	4
Fig. 7. Variation of lift and drag forces with pitch angle of attack.....	5
Fig. 8. Lift, drag and pitch moment characteristics of the NRL-UUV. ....	5
Fig. 9. Variation of side and drag forces with side slip. ....	6
Fig. 10. Side, drag and yaw moment characteristics of the NRL-UUV. ....	6
Fig. 11. Surface pressure distribution on NRL-UUV, $\dot{\alpha} = 15^\circ/\text{s}$ , $V = 0$ .....	7
Fig. 12. Kinematics for a flapping deforming fin, $f = 0.9091\text{Hz}$ . ....	8
Fig. 13. Thrust and lift production from a tandem flapping fins, $f = 0.9091\text{Hz}$ , $V = 0\text{kts}$ , $x_{\text{rear}} = 6^\circ$ . ....	8
Fig. 14. Thrust and lift production from a tandem flapping fins, $f = 0.9091\text{Hz}$ , $V = 0\text{kts}$ , $x_{\text{rear}} = 3^\circ$ . ....	8
Fig. 15. Particle traces released from the front fin.....	9
Fig. 16. Kinematics for a flapping deforming fin producing forward thrust, $f = 1.818\text{Hz}$ . ....	9
Fig. 17. Thrust and lift production from a flapping fin, $f = 1.818\text{Hz}$ , $V = 0\text{kts}$ .....	10
Fig. 18. Thrust and lift production from tandem flapping fins, $f = 1.818\text{Hz}$ , $V = 0.5\text{kt}$ .....	11
Fig. 19. Thrust and lift production from tandem flapping fins, $f = 1.818\text{Hz}$ , $V = 1\text{kt}$ .....	11
Fig. 20. Variation of Mean thrust with phasing of the rear fin, $V = 1\text{kt}$ .....	12
Fig. 21. Effect of phasing on the time history of thrust produced by the rear fin, $V = 1\text{kt}$ . ....	12
Fig. 22. Thrust and lift production from tandem flapping fins, $f = 1.818\text{Hz}$ , $V = 1\text{kt}$ , $\delta = -43.6^\circ$ . ....	12
Fig. 23. Instantaneous surface pressure distribution on NRL-UUV, $V = 1\text{kt}$ , $\delta = -43.6^\circ$ . ....	13
Fig. 24. Surface pressure distribution on NRL-UUV at $t = 1.208\text{s}$ , $V = 1\text{kt}$ , $\delta = -43.6^\circ$ . ....	14
Fig. 25. Surface pressure distribution on the flapping fins, $t = 1.208\text{s}$ . ....	14

Fig. 26. Surface pressure distribution on the front fin, $t = 1.143s$ .....	15
Fig. 27. Effect of inflow velocity on thrust and lift production from a single flapping fin .....	16
Fig. 28. Variation of unsteady thrust production from the flapping fins with vehicle speed. ....	16
Fig. 29. Effect of vehicle speed on the mean thrust produced by the fins .....	16
Fig. 30. Inflow conditions for the front and rear fins at $t = 1.208s$ , $V = 1kt$ , $\delta = -43.6^\circ$ .....	17
Fig. 31. Spanwise component of vorticity at $z = 6.5''$ , $V = 1kt$ , $\delta = -43.6^\circ$ .....	17
Fig. 32. Particles traces just near stroke reversal of the front and rear fins into upstroke .....	18
Fig. 33. Particles traces after 4 flapping cycles .....	19
Fig. 34. Biasing of the rear fin .....	20
Fig. 35. Thrust and lift variation with rear fin biasing, $V = 1kt$ .....	20
Fig. 36. Configuration of the vehicle with front fin fixed .....	20
Fig. 37. Thrust and lift variation with the front fin fixed, $V = 1kt$ .....	21
Fig. 38. Thrust and lift variation with the front fin fixed, $V = 0.5kt$ .....	21
Fig. 39. Kinematics for a flapping deforming fin producing lift, $f = 4.62\text{Hz}$ .....	21
Fig. 40. Thrust and lift variation with lift kinematics, $f = 4.62\text{Hz}$ , $V = 0\text{kts}$ .....	22
Fig. 41. Kinematics for a flapping deforming fin producing lift, $f = 1.4\text{Hz}$ .....	22
Fig. 42. Thrust and lift variation with lift kinematics, $f = 1.4\text{Hz}$ , $V = 0\text{kts}$ .....	22
Fig. 43. Kinematics for a flapping deforming fin producing reverse thrust, $f = 1.765\text{Hz}$ .....	23
Fig. 45. Forces and moments on the NRL-UUV .....	25
Fig. 46. Forces and moments on the NRL-UUV undergoing a yaw maneuver .....	25
Fig. 47. Trajectory of NRL-UUV during a yaw turn .....	25
Fig. 48. Surface pressure distribution on the flapping fins during the yaw maneuver .....	27
Fig. 49. Vehicle configuration with symmetric fin orientation .....	27
Fig. 50. Thrust and lift production for a vehicle with symmetric fin orientation, front fin with forward thrust kinematics and rear fin with reverse thrust kinematics, $V = 1kt$ .....	28
Fig. 51. Thrust and lift production for a vehicle with symmetric fin orientation, front fin with forward thrust kinematics and rear fin with reverse thrust kinematics, $V = 0.5kt$ .....	28
Fig. 52. Surface pressure distribution on vehicle with symmetric fin orientation, $t = 1.215s$ , $V = 1kt$ .....	29
Fig. 53. Effect of moment of inertia on the yaw turn for NRL-UUV with symmetric fin orientation .....	30
Fig. 54. Kinematics for a flapping deforming fin producing negative lift, $f = 1.395\text{Hz}$ .....	30
Fig. 55. Thrust and lift variation with cupped kinematics, $f = 1.395\text{Hz}$ , $V = 0\text{kts}$ .....	31
Fig. 56. Trajectory of the NRL-UUV during a dive maneuver, $f = 1.395\text{Hz}$ .....	31

## Development of a 4-fin Bio-Inspired UUV: CFD studies

### INTRODUCTION

Current unmanned underwater vehicles (UUVs) operate with propellers and conventional control surfaces and are designed for cruise. These are not well suited for operating in cluttered, near shore environments where maneuvering and controllability at low speed, unsteady flow are important. Flapping and deforming fins may provide significant low-speed maneuvering, obstacle avoidance and position keeping capabilities for future UUV operations. Oscillatory deforming wing and fin motion for propulsive force generation is common in birds and fishes but uncommon in man-made vehicles. This mode of propulsion, which also might not need body undulation, has many applications, such as submersibles propulsion, maneuvering, and flow control which are of interest to the UUV hydrodynamic community and unconventional aerodynamics of Micro Aerial Vehicles (MAV) and the study of aircraft flutter for the aerodynamic community. We address the question here of the importance of flapping surface deformation to the magnitude of propulsive force generation.

To confront the issue of low-speed maneuverability in the presence of ocean currents and near-shore obstacles, flapping fin mechanisms have been studied to understand how certain aquatic animals achieve their high levels of controllability. Blake [1] determined that in low-speed operations labriform motion (using pectoral fin oscillation) is more efficient for maneuvering than carangiform motion (using body and caudal fin undulation). This result indicates that a flapping pectoral fin can be mounted on a rigid UUV hull without sacrificing low-speed maneuverability. Kato et al. [2] and Ando et al. [3] have developed both lift-based and drag-based deformable pectoral fins for use on UUVs. Tangorra et al. [4] have developed a flapping fin based on the bluegill sunfish. They have used CFD simulations and proper orthogonal decomposition analysis to retain the first few modes without replicating the entire fin motion. We have previously carried out 3-D unsteady computations to determine the flow and force production time history of rigid flapping insect wings [5] and flapping and deforming pectoral fins [6]. Those results were compared with and showed good agreement with experimental results. The objectives of this study are to investigate force production of deformable flapping fins and to integrate these fins onto an unmanned underwater vehicle (UUV) capable of superior low-speed maneuverability and hover. Three-dimensional unsteady computations of flapping foil propulsion for bio-inspired UUVs are carried out. The flow past a test vehicle, NRL-UUV, was computed varying the flexibility of the fin, the amplitude of the flapping and starting location of the down stroke. These simulations were performed in order to evaluate the hydrodynamic performance of the vehicle and to assist the controller development of the vehicle. In our previous work, we showed that active control over the curvature of the robotic pectoral fins was necessary to achieve precise low-speed maneuverability of UUVs in highly time-varying external force environments [7]. Design and construction of such a fin, and testing of this fin on a two-fin vehicle have demonstrated the success of this strategy in achieving the force production and vehicle maneuvering capabilities necessary for operation in these challenging environments [8][9].

Licht et al. [10] designed a large ( $2\text{m} \times 0.5\text{m} \times 0.5\text{m}$ ) UUV with four rigidly flapping fins with pitch and heave motions and studied pitch biasing as an effective method of vehicle control

at hover. In this research effort, we describe the development of a four-fin vehicle capable of carrying a larger payload, and able to operate at higher forward speed with better pitch control and turning characteristics compared to our two-fin demonstration vehicle. Several cross sections were considered and based on the minimum drag a nearly elliptical cross-section with a smooth leading and trailing sections was obtained. The hydrodynamic characteristics of a newly built prototype vehicle at NRL consisting of four fins were computed for a range of operational conditions and a dynamic mode of this vehicle was created for the development of a controller. Detailed parametric studies were carried out varying several physical and kinematic parameters, such as separation of the two fins, the phasing of the rear fin with respect to the front fin, the stroke amplitudes of the fins, to mention a few. The kinematics corresponding to the fin producing a forward thrust was used to perform parametric studies for a vehicle moving at 1kt. The 3-D unsteady flow solver is coupled to a 6-dof model to simulate a yaw maneuver of the vehicle using different kinematics for the right and left fins. The computational results are obtained using an unstructured grid based Navier-Stokes solver, *feflo*, which is briefly described next.

## THE INCOMPRESSIBLE FLOW SOLVER

The governing equations employed are the incompressible Navier-Stokes equations in Arbitrary Lagrangian-Eulerian (ALE) formulation which are written as

$$\frac{d\mathbf{v}}{dt} + \mathbf{v}_a \cdot \nabla \mathbf{v} + \nabla p = \nabla \cdot \boldsymbol{\sigma}, \quad (1)$$

$$\nabla \cdot \mathbf{v} = 0, \quad (2)$$

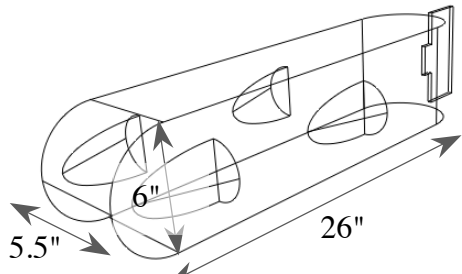
where  $p$  denotes the pressure,  $\mathbf{v}_a = \mathbf{v} - \mathbf{w}$  the advective velocity vector, where  $\mathbf{v}$  is the flow velocity and  $\mathbf{w}$  is the mesh velocity  $w$  and the material derivative is with respect to the mesh velocity  $\mathbf{w}$ . Both the pressure  $p$  and the stress tensor  $\boldsymbol{\sigma}$  have been normalized by the (constant) density  $\rho$  and are discretized in time using an implicit time stepping procedure. Thus the equations are Eulerian for zero mesh velocity and Lagrangian if the mesh velocity is the same as the flow velocity. The present time-accurate flow solver is discretized in space using a Galerkin procedure with linear tetrahedral elements. The details of the flow solver have already been discussed extensively elsewhere, Ramamurti *et. al.* [6,7], in connection with successfully validated solutions for numerous 2-D and 3-D, laminar and turbulent, steady and unsteady flow problems.

## RESULTS AND DISCUSSION

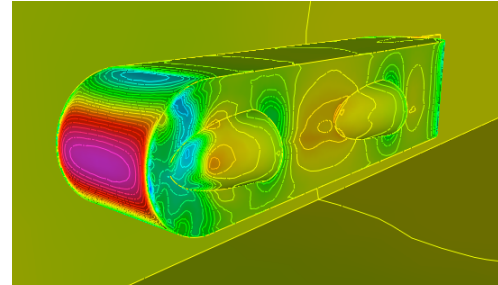
### Vehicle Selection:

Ramamurti *et al.* [7] have computed the unsteady flow past a UUV with flapping fins. Several parametric studies were performed for an isolated flapping fin and were demonstrated using a vehicle that carries two actively controlled curvature fins. In order to carry a larger payload, and to be able to operate at higher forward speed with better pitch control and turning characteristics compared to our two-fin vehicle, we considered a four-fin vehicle. Several cross sections were considered and the drag was minimized for a flow velocity of 1kt. The first such configuration is shown in Fig 1a and is 26" long with a rectangular cross section of 6" high ×

5.5" wide. The leading and trailing edge sections are semi-circular sections. The pressure distribution on this configuration is shown in Fig. 1b and the total drag is 1.51N. This configuration was modified to have a rectangular cross section of 4.5" high  $\times$  5.2" wide. The leading and trailing edge sections were elliptical and the top and bottom sections of the vehicle are semi-circular producing a vehicle 26" long and 9" high. The modified configuration and the pressure distribution are shown in Fig. 2. The drag force for this configuration is reduced 1.01N. In order to further reduce the drag, the fin mounting caps on the sides of the vehicle were removed. The resulting configuration is shown in Fig. 3 and has a reduced drag of 0.32N. The fins are then mounted on this configuration using rectangular slots on the sides which increased the drag to 0.84N as shown in Fig. 4. Next, an elliptical cross section configuration was considered with 3.5" and 7" as the minor and major axes, respectively. The nose and the tail sections were also made of elliptical caps. The minor axis of these caps was increased from 3.5" to 5.25" and further to 7.5" to study the effect of streamlining the nose section. As the minor axis is increased from 3.5" to 5.25", the drag reduced from 0.67N to 0.6N and further increase in the minor axis to 7" increased the drag further to 0.67N due to increase in surface area. Figure 5 shows the configuration and the pressure distribution corresponding to the nose cap with 5.25" as the minor axis. The fully extended fins and the boxes that house the servos were then added to the body and the resulting configuration, called the NRL-UUV is shown in Fig. 6. The overall length of this vehicle is 17.25" and the drag for this configuration is 0.44N.

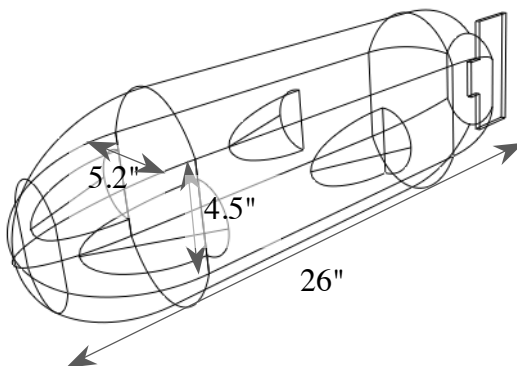


a. vehicle configuration

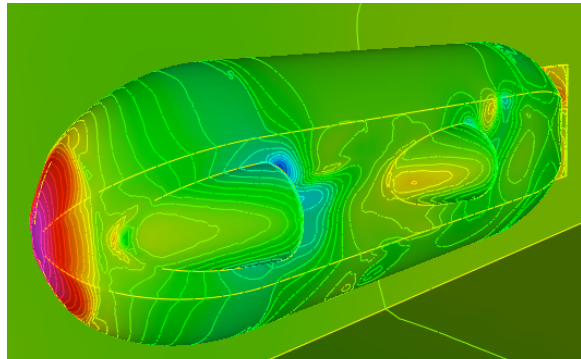


b. surface pressure distribution

Fig. 1. Flow past a rectangular cross section vehicle.

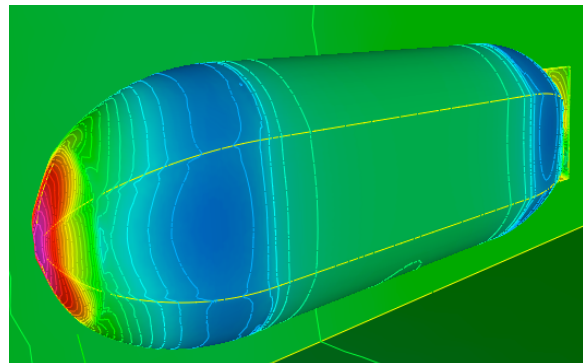
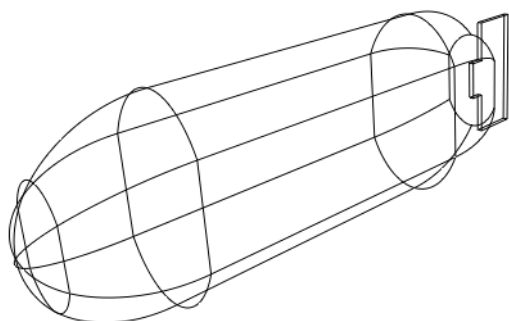


a. vehicle configuration



b. surface pressure distribution

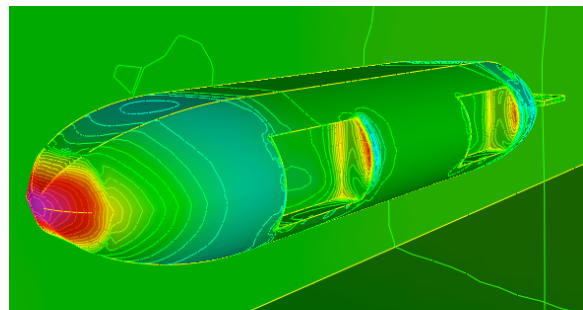
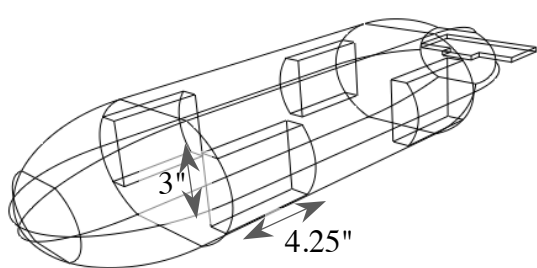
Fig. 2. Flow past a modified rectangular cross section vehicle.



a. vehicle configuration

Fig. 3. Flow past a modified rectangular cross section vehicle without mounting caps.

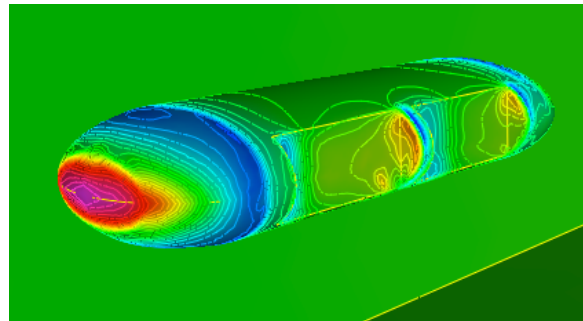
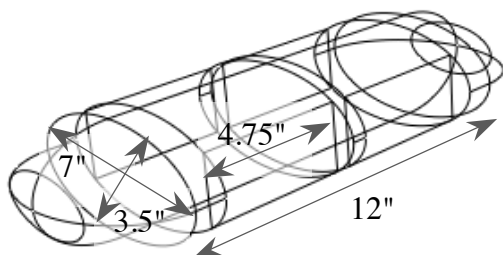
b. surface pressure distribution



a. vehicle configuration

Fig. 4. Flow past a modified rectangular cross section vehicle with side slots.

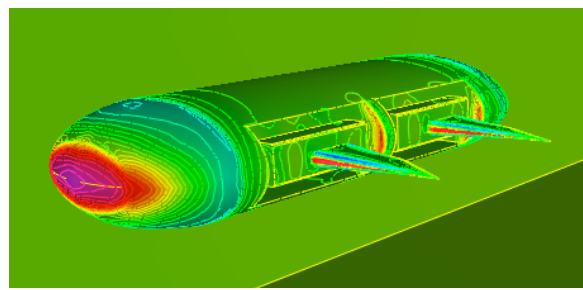
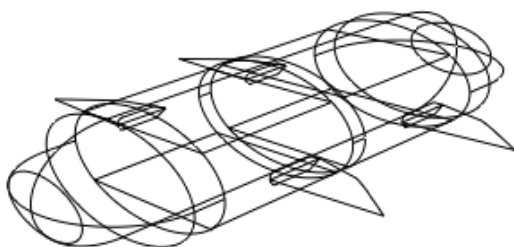
b. surface pressure distribution



a. vehicle configuration

Fig. 5. Flow past a vehicle with elliptical cross section.

b. surface pressure distribution



a. vehicle configuration

Fig. 6. Flow past a vehicle with elliptical cross section with fins.

b. surface pressure distribution

The computed forces ( $F_x, F_y, F_z$ ) are transformed to their respective drag, lift and side forces ( $D, L, N$ ) which are normalized using the free stream velocity  $V$ , the density of water  $\rho$ , and the area of the body  $A_b$ . The area of the body is taken to be half the wetted area of the body,  $A_w = 396.1$  sq in. The total wetted area of all the four fins is 39.4 sq in.

$$C_D = \frac{D}{\frac{1}{2} \rho V^2 A_b}, \quad C_L = \frac{L}{\frac{1}{2} \rho V^2 A_b} \quad \text{and} \quad C_N = \frac{N}{\frac{1}{2} \rho V^2 A_b} \quad (2 \text{ a-c})$$

The moments are further normalized by the hydraulic diameter of the elliptical cross section,  $d_h = 2A_{CS}/P$ , where  $A_{CS}$  and  $P$  are the area and the perimeter of the elliptical cross section, respectively.

### Effect of angle of attack:

The steady flow hydrodynamic characteristics of this configuration is next obtained for a vehicle speed,  $V = 1\text{kt}$ , and for various angles of attack,  $\alpha$ , in the range of  $0^\circ$  to  $30^\circ$  and side slip angle,  $\beta$ , in the range of  $0^\circ$  to  $15^\circ$ . Figure 7 shows the variation of the total lift and drag on the body and fins with pitch angle of attack. The lift force varies linearly and the drag force varies in a quadratic manner with angle of attack, as expected. At  $\alpha = 0^\circ$ , the drag force on the vehicle is approximately 0.44 N, yielding  $C_{D0}$  of  $6.5 \times 10^{-3}$ . The variation of lift, drag and pitch moment coefficients with angle of attack are shown in Fig. 8.

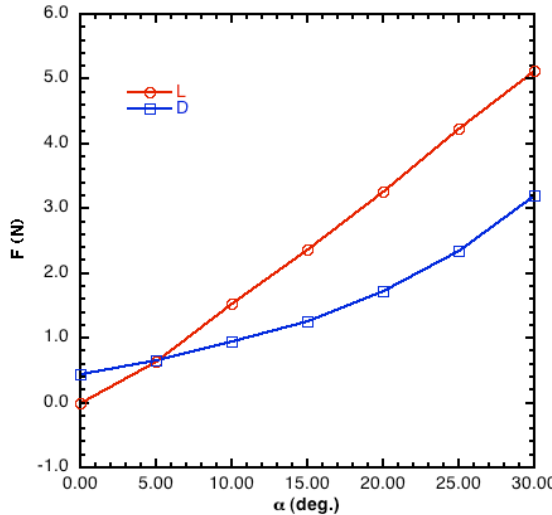
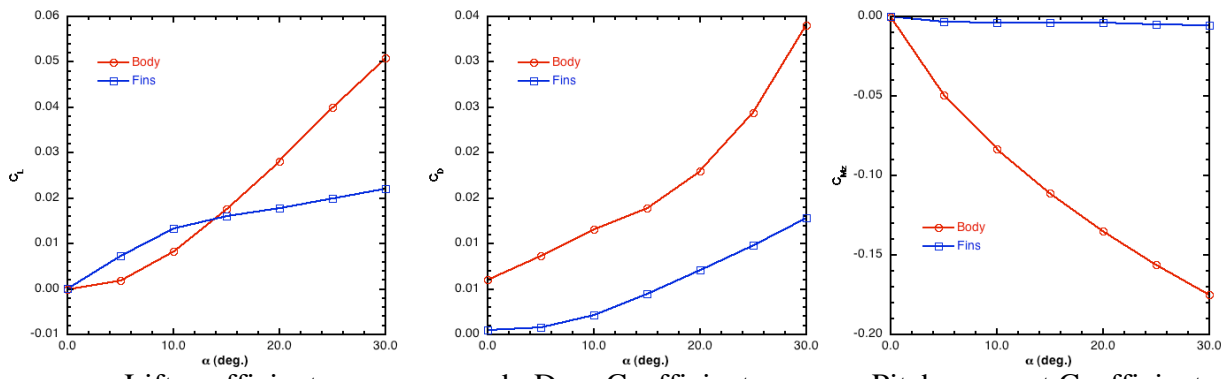


Fig. 7. Variation of lift and drag forces with pitch angle of attack.



a. Lift coefficient      b. Drag Coefficient      c. Pitch moment Coefficient

Fig. 8. Lift, drag and pitch moment characteristics of the NRL-UUV.

### Effect of Side Slip angle:

In order to assess the characteristics of the vehicle with respect to the side slip angle, the flow past the vehicle was simulated over a range  $0^\circ$  to  $15^\circ$ . Figure 9 shows the variation of the side and drag forces on the vehicle. As the side slip angle is increased from  $0^\circ$  to  $15^\circ$ , it can be seen that the side force increases from nearly zero to  $0.23\text{N}$  and drag force increases from  $0.44\text{N}$  to  $0.54\text{N}$ .

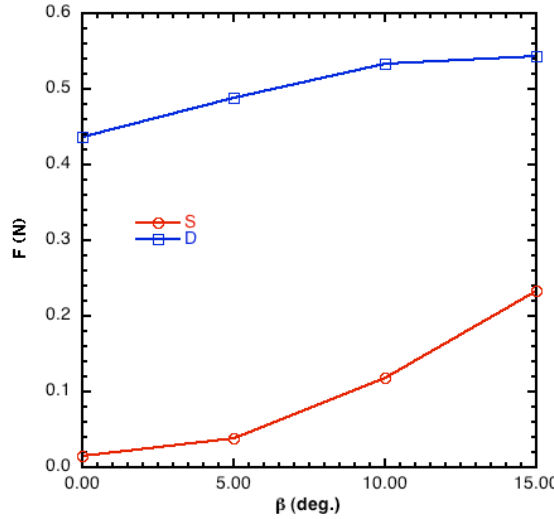
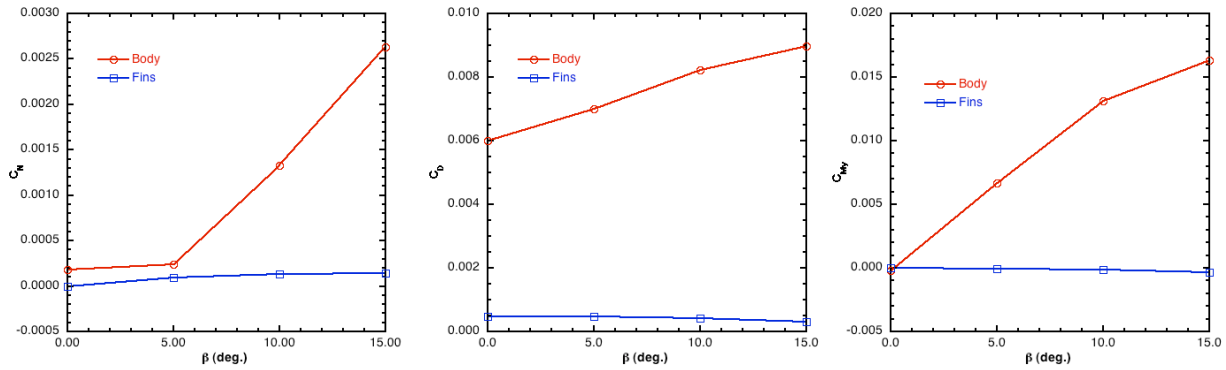


Fig. 9. Variation of side and drag forces with side slip.



a. Side force coefficient      b. Drag Coefficient      c. Yaw moment Coefficient

Fig. 10. Side, drag and yaw moment characteristics of the NRL-UUV.

### Turn rate characteristics:

In order to obtain the hydrodynamic damping coefficients, the vehicle was subjected to a constant turn rate ( $\dot{\gamma}$ ,  $\dot{\beta}$ ,  $\dot{\alpha}$ ) about each of the axes ( $x, y, z$ ), individually. Two rates of  $15^\circ$  and  $30^\circ$  per second were selected for this study. The vehicle was stated impulsively in a stagnant medium, and the time variation of the forces and moments showed that a steady state is achieved after 2 s of simulation. The moments about the rotational axes showed a quadratic behavior with respect to the constant turn rate, as expected and is shown in Table. 1. For instance, as the yaw rate  $\dot{\beta}$ , is increased for 15 to 30 deg/s, the yaw moment  $M_y$ , increases in magnitude nearly four fold from  $2.16\text{E-}04$  to  $8.56\text{E-}04$ . The surface pressure distribution over the vehicle for  $\dot{\alpha} =$

15°/s, at steady state is shown in Fig. 11. These vehicle hydrodynamic characteristics together with the force production of isolated flapping fins for specific sets of kinematics, called gaits, were incorporated in the development of the vehicle controller.

Turn rate, $\dot{\gamma}$ , $\dot{\beta}$ , $\dot{\alpha}$ (deg/s)	$M_x$ (N-m)	$M_y$ (N-m)	$M_z$ (N-m)
15	-2.187E-03	-2.160E-04	-1.544E-03
30	-8.755E-03	-8.563E-04	-6.190E-03

Table 1. Turn rate characteristics.

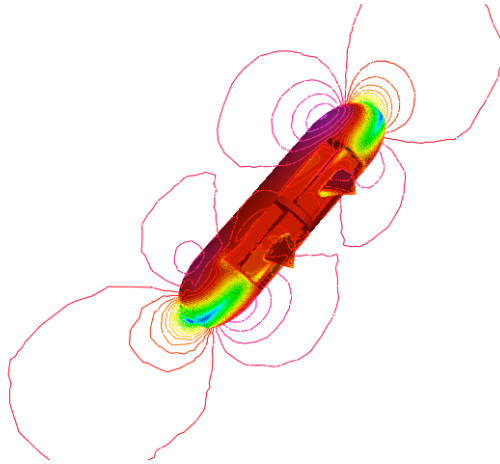
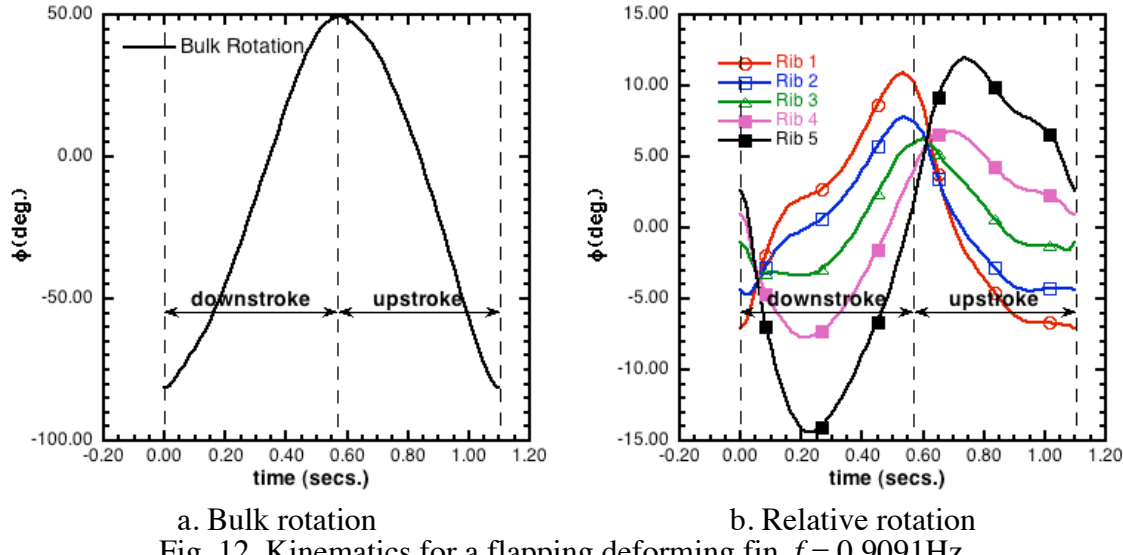
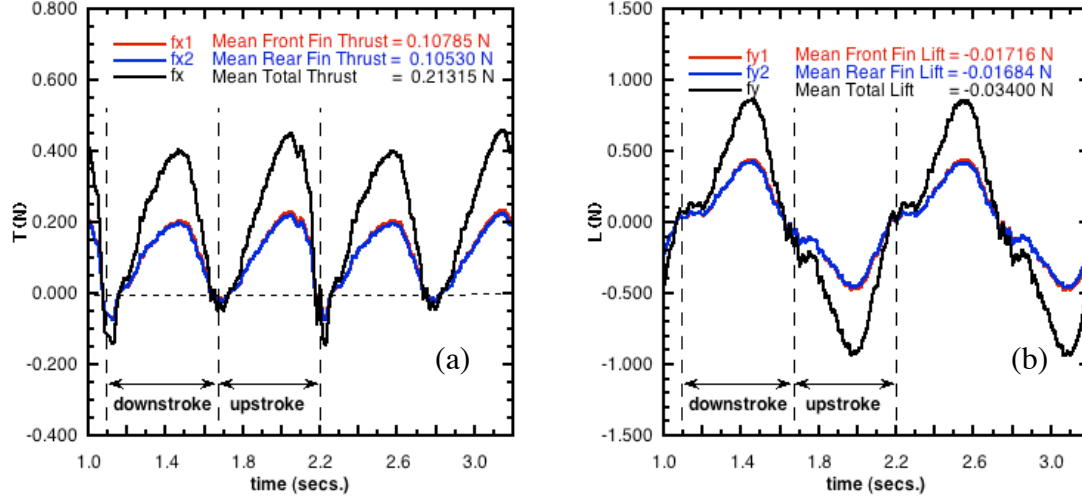
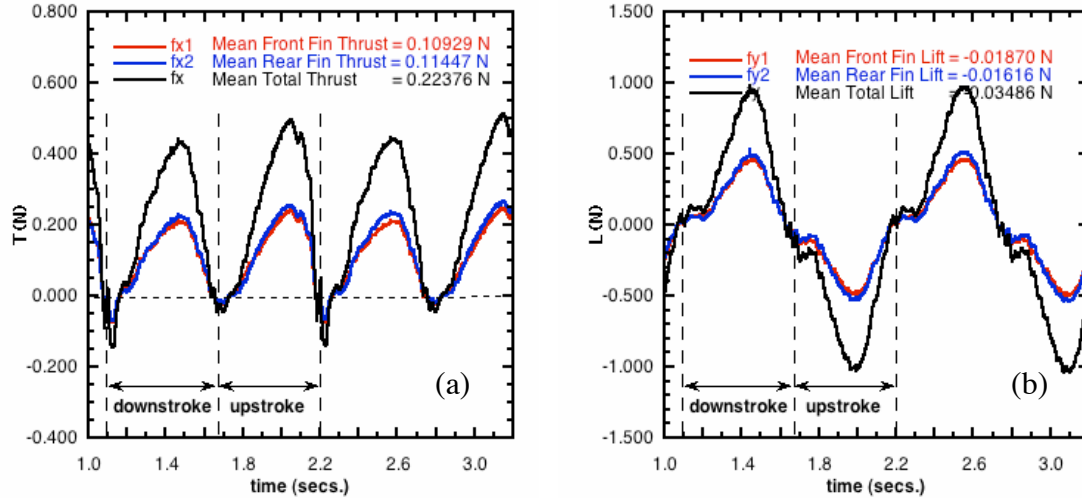


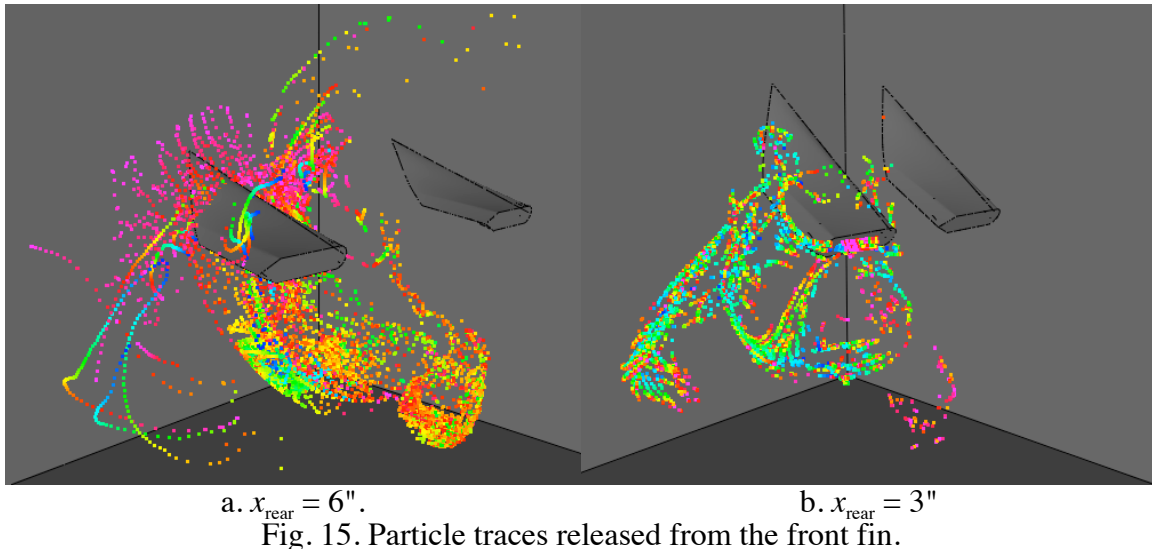
Fig. 11. Surface pressure distribution on NRL-UUV,  $\dot{\alpha} = 15^\circ/\text{s}$ ,  $V = 0$ .

### Effect of axial separation of the fins:

Initial studies were conducted to understand the effect of axial separation of the rear fin from the front fin on the thrust and lift production using two isolated tandem flapping fins. For this study, two separation distances,  $x_{\text{rear}}$  of 3" and 6" were considered. The deforming motion of the flapping fin is obtained by prescribing the motion of five control points located at the tip of the ribs as described in Ramamurti et al. [7]. The kinematics of the ribs is decomposed into a bulk rotation about the fin axis of rotation and a supplemental relative rib rotation, and has a bulk rotation amplitude of 130° at a flapping frequency of 0.91 Hz. Figure 12 shows this set of kinematics which was experimentally obtained and used in the previous validation study [7].

The separation between the front and the rear fins was initially set to 6". The computed results for the time history of thrust and lift production from the two fins are shown in Fig. 13. These results show that both thrust and lift production from the rear fin is almost the same as that of the front fin. This suggests that the rear fin is not getting the benefit of any wake capture effect resulting from the front fin. Particle traces released near the leading and trailing edges of the front fin show that the resulting wake impinges only a small portion of the fin tip region. Hence, the separation distance was reduced to 3". The thrust and lift production for this case is shown in Fig. 14 and shows only a modest gain in thrust from the rear fin. One reason for this may be due to the fact that the fins are flapping in stagnant water and a positive inflow will be

Fig. 12. Kinematics for a flapping deformable fin,  $f = 0.9091\text{Hz}$ .Fig. 13. Thrust and lift production from a tandem flapping fins,  $f = 0.9091\text{Hz}$ ,  $V = 0\text{kts}$ ,  $x_{\text{rear}} = 6''$ .Fig. 14. Thrust and lift production from a tandem flapping fins,  $f = 0.9091\text{Hz}$ ,  $V = 0\text{kts}$ ,  $x_{\text{rear}} = 3''$ .



able to carry the wake into the rear fin. The particle traces for these two cases are shown in Fig. 15 suggest that although the wake from the front fin impinges on the rear fin, the phasing may not be optimum.

## Parametric Studies:

Further parametric studies were performed varying the phasing of the rear fin with respect to the front fin and the vehicle speed. For this study, the fins were mounted on the NRL-UUV, described before. The axial separation of the rear fin from the front fin is 4.35". An improved set of kinematics producing forward thrust with the fin flapping at 1.82 Hz and a reduced bulk amplitude of 83.3° was used for this study and is shown in Fig. 16. Results from the computations on an isolated fin, Fig. 17, show that the mean thrust using this new set is 0.21 N compared to 0.11 N using the previous set of kinematics.

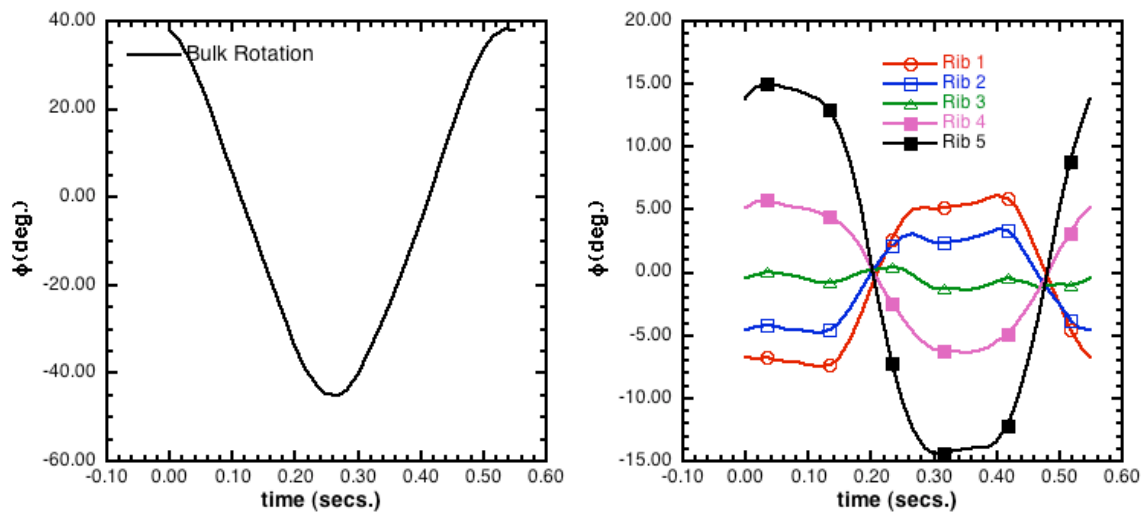


Fig. 16. Kinematics for a flapping deforming fin producing forward thrust,  $f = 1.818\text{Hz}$ .

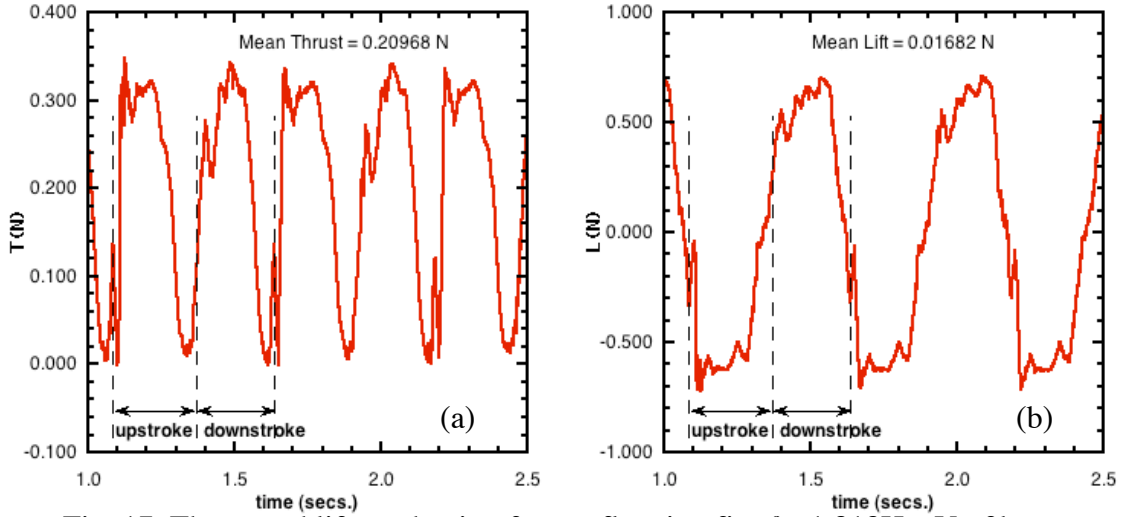


Fig. 17. Thrust and lift production from a flapping fin,  $f = 1.818\text{Hz}$ ,  $V = 0\text{kts}$ .

Next, the front and the rear fins were flapped in phase with the vehicle moving at  $V = 0.5\text{kts}$ . The vehicle configuration for these parametric studies used a symmetry plane with half the vehicle and single front and rear fin. The initial computational mesh consists of 1.08 M points and 6.11 M tetrahedral elements. The mean thrust and lift from the simulation averaged over 5 flapping cycles is shown in Fig. 18. In this case, the front fin produces a mean thrust of 0.123 N and the rear fin produces 0.129 N. Again, as in the previous hover condition, there is no significant increase in the thrust produced by the rear fin. The total mean thrust on the vehicle is 0.17 N, implying that the flapping fins produce more thrust to overcome the drag on the vehicle. The mean lift from the front and rear fins are 0.02N and 0.03N, respectively, and the total mean lift is 0.03N. As the vehicle velocity is increased to 1kt, the force production from the rear fin is 0.073 N compared to 0.04 N from the front fin as shown in Fig. 19. From this figure it is clear that after stroke reversals, the rear fin produces additional thrust arising from the wake capture effect. This is similar to the effect that is evidenced in the hovering fruitfly, shown in previous studies by Dickinson et al. [11] and Ramamurti and Sandberg [5]. Even with this additional thrust from the rear fin, it is not enough to overcome the drag on the vehicle. The total mean drag on the vehicle is 0.19N. Hence, additional parametric studies varying the phasing of the rear fin was performed.

### Effect of Phasing of the Rear Fin:

For this study, the kinematics producing forward thrust was used. This kinematics was obtained experimentally measured at 33 time intervals at a flapping frequency of 1.818 Hz, shown in Fig. 16. The phasing of the rear fin was modified by altering the starting time interval with respect to the front fin. The shift in time intervals that were chosen are  $\{ \pm 2, \pm 4, \pm 8, 17 \}$ , resulting in a phase shift of  $\delta = \{ \mp 21.8^\circ, \mp 43.6^\circ, \mp 87.3^\circ, -174.6^\circ \}$ , respectively. Unsteady flow computations were performed over these configurations for several flapping cycles, and the results were time averaged over 5 flapping cycles. The variation of the mean thrust from the front and rear fins is shown in Fig. 20. The front fin produces a constant thrust of nearly 0.04N. The rear fin produces 0.073N of mean thrust, a factor of nearly 1.8 times of the front fin when flapped in phase. This mean thrust increases to a value of 0.083N when the phasing is lagged by

43.6°, a factor of nearly 2.1. As the phasing is lagged further, the thrust produced during the mid stroke reduces, resulting in a mean thrust of 0.059N at 87.3° and 0.014N at 174.6°. A phase lead of 43.6° results in a reduced mean thrust of 0.069N. The reason for this additional thrust at  $\delta = -43.6^\circ$ , is due to the capture of the wake that is produced by the front fin. This reduces the loss of thrust just before and after the stroke reversals, as shown in Fig. 21, although the peak thrust at the beginning of the upstroke is reduced. For clarity, only few of the time histories are shown in Fig. 21. When the rear fin leads the front fin by 43.6°, the peak thrust after the stroke reversal is delayed leading to a reduced mean thrust.

The thrust and lift production from the flapping fins when the rear is lagged by 43.6° is shown in Fig. 22. The instantaneous surface pressure distribution throughout the flapping cycle at instants where the thrust and the lift reach near extrema is shown in Fig. 23. The additional thrust from the rear fin can be analyzed from the surface pressure distribution. Figure 24 shows the surface pressure distribution on the vehicle at  $t = 1.208s$  when the thrust from the rear fin reaches a maximum after the stroke reversal to the upstroke. The orientation of the front and the

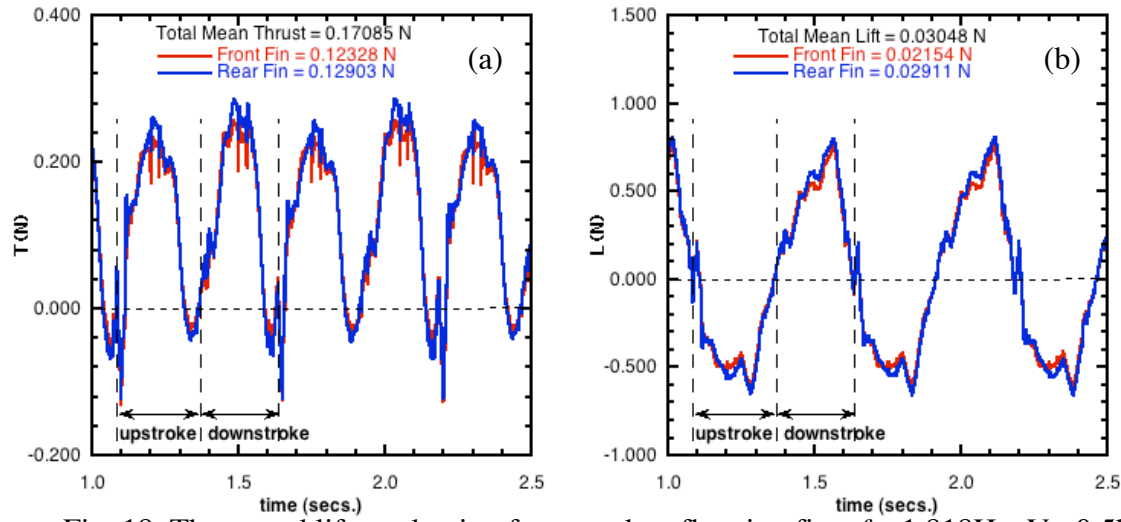


Fig. 18. Thrust and lift production from tandem flapping fins,  $f = 1.818\text{Hz}$ ,  $V = 0.5\text{kt}$ .

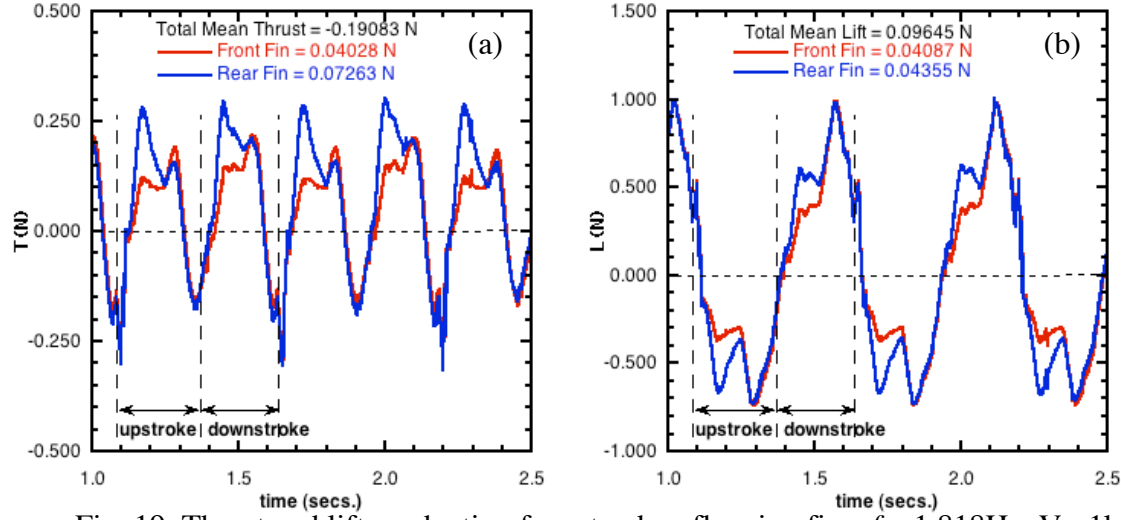


Fig. 19. Thrust and lift production from tandem flapping fins,  $f = 1.818\text{Hz}$ ,  $V = 1\text{kt}$ .

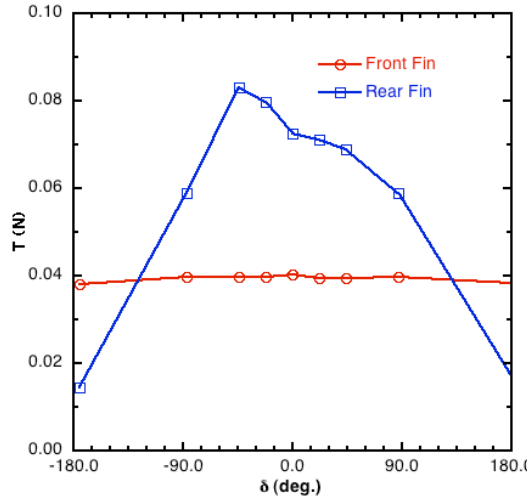


Fig. 20. Variation of Mean thrust with phasing of the rear fin,  $V = 1\text{kt}$ .

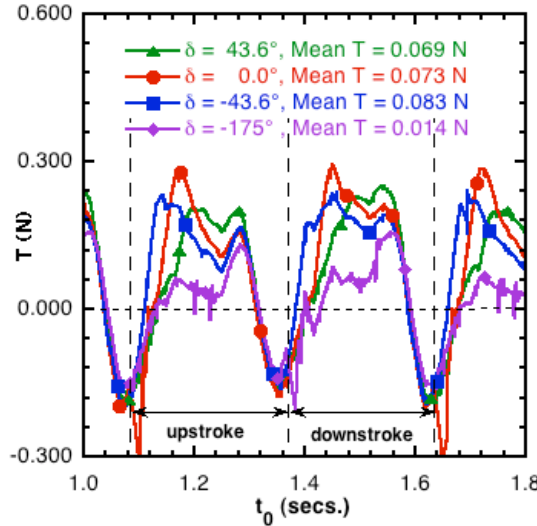


Fig. 21. Effect of phasing on the time history of thrust produced by the rear fin,  $V = 1\text{kt}$ .

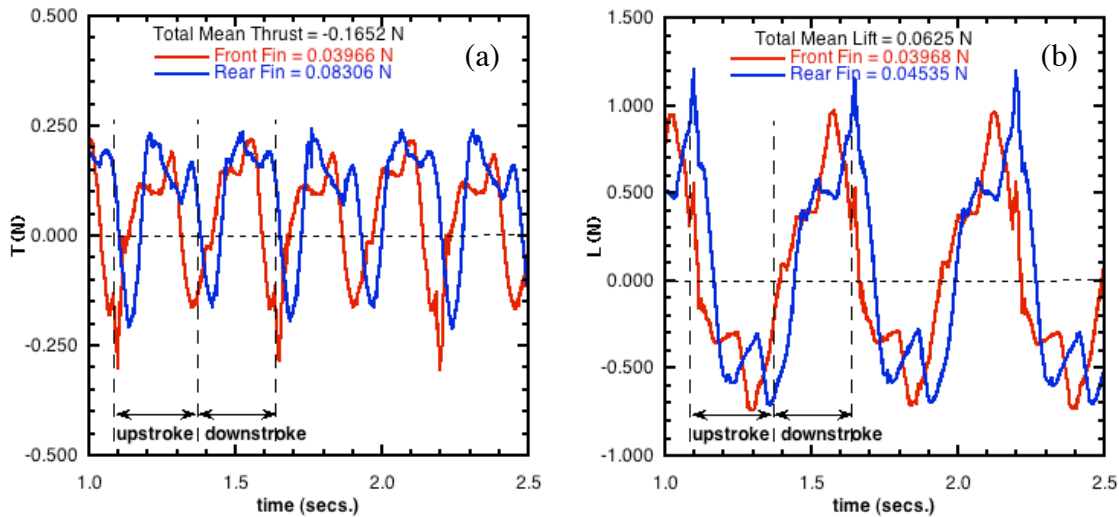


Fig. 22. Thrust and lift production from tandem flapping fins,  $f = 1.818\text{Hz}$ ,  $V = 1\text{kt}$ ,  $\delta = -43.6^\circ$ .

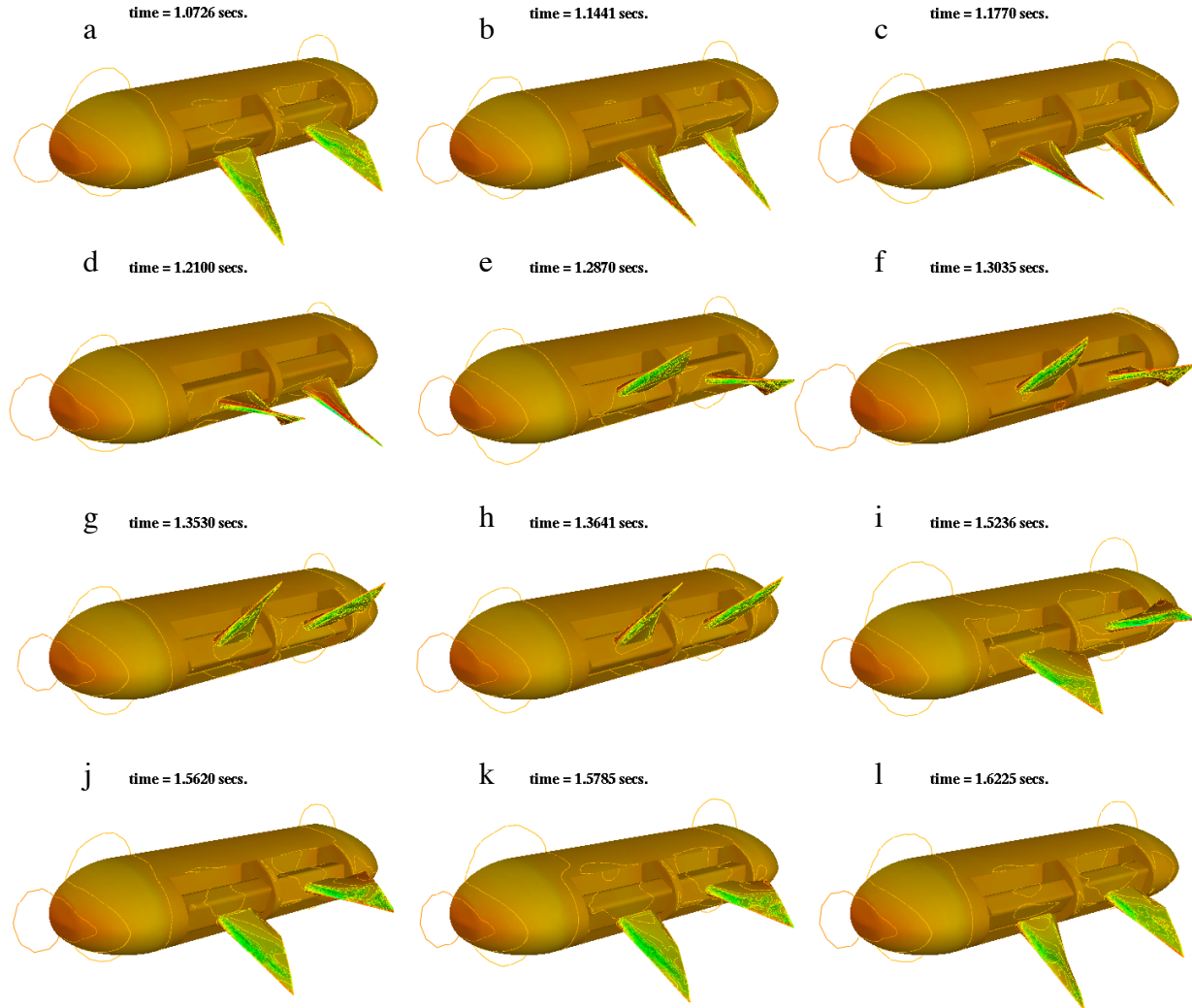


Fig. 23. Instantaneous surface pressure distribution on NRL-UUV,  $V = 1\text{kt}$ ,  $\delta = -43.6^\circ$ , a) stroke reversal of front fin, b) after stroke reversal of rear fin, c) thrust peak of the front fin after reversal, d) thrust peak of rear fin after reversal, e) peak thrust of front fin, f) minimum lift of front fin, g) maximum thrust rear fin, h) minimum lift of rear fin, i) maximum thrust of rear fin during downstroke, j) maximum thrust of front fin during downstroke, k) maximum lift of front fin during downstroke and l) maximum lift of rear fin during downstroke.

rear fins due to the phase lag is shown in this figure. A close look at the pressure distribution on the top and bottom surfaces at this instant, Fig. 25a-d, shows that the pressure in the leading edge region in the top surface of the rear fin, Fig. 25c, is much higher compared to that of the front fin, Fig. 25a. Also, the pressure in the leading edge region on the bottom surface, Fig. 25d is much lower compared to that of the front fin, Fig. 25b. In addition to this, the orientation of the rear fin is such that the net force is directed in the  $x$ -direction. In comparison, the surface pressure distribution on the front fin at the same orientation, at  $t = 1.143\text{s}$ , exhibits that a much reduced pressure on the top surface and higher minimum pressure on the bottom surface of the fin, as shown in Fig. 26.

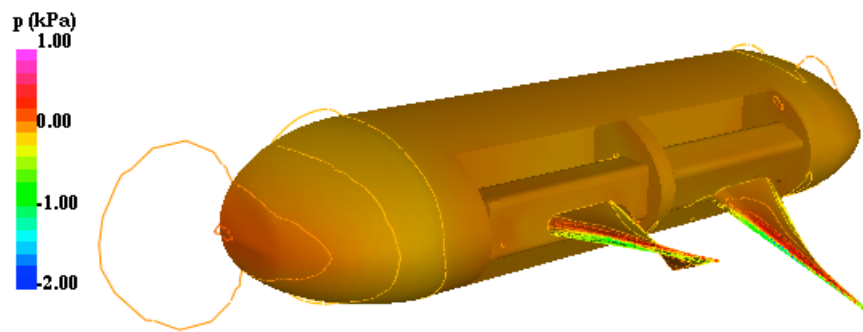


Fig. 24. Surface pressure distribution on NRL-UUV at  $t = 1.208s$ ,  $V = 1kt$ ,  $\delta = -43.6^\circ$ .

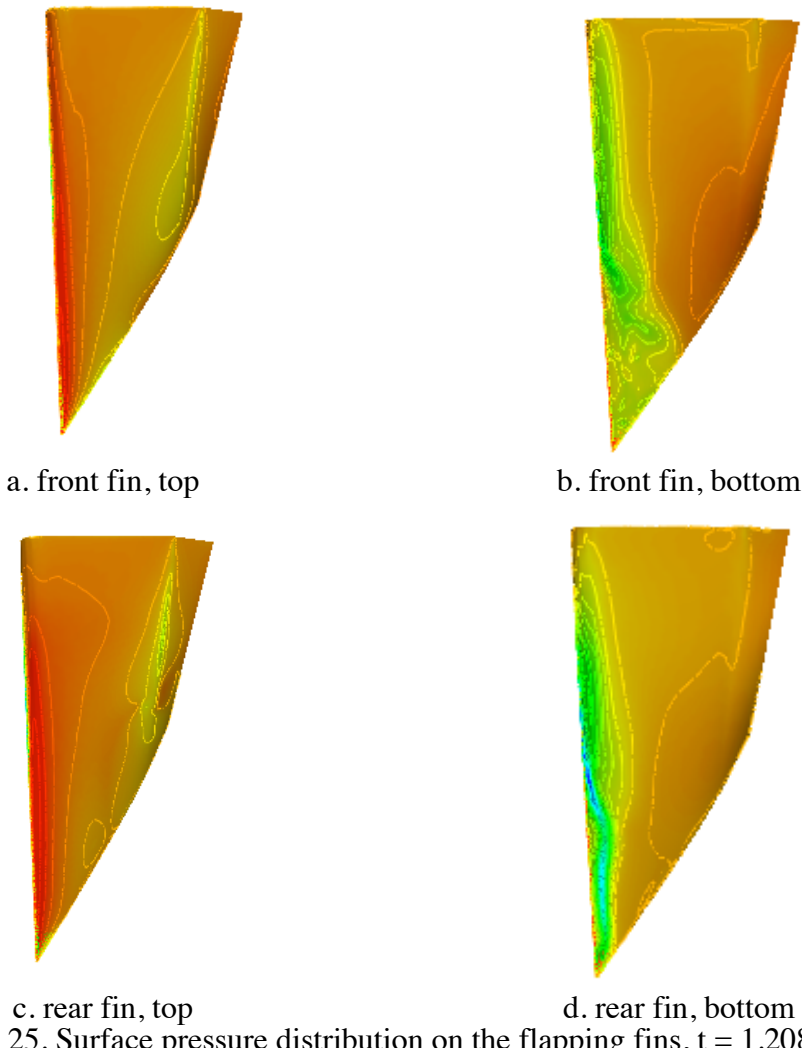


Fig. 25. Surface pressure distribution on the flapping fins,  $t = 1.208s$ .

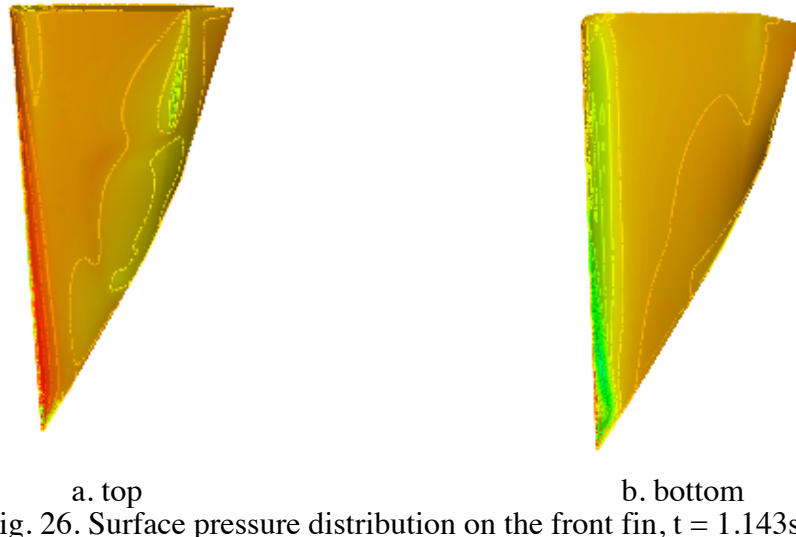


Fig. 26. Surface pressure distribution on the front fin,  $t = 1.143s$ .

### Effect of Vehicle Speed:

The effect of the incoming flow velocity on the thrust and lift production was tested on an isolated fin flapping according to the kinematics described in Fig. 16. As the flow velocity is increased from 0kts to 1kt, the mean thrust produced by the fin reduces from 0.21N to 0.04N, as shown in Fig. 27a; the mean thrust at 0.5kts is nearly 0.12N. The mean lift also increases from 0.017N to 0.04N, Fig. 27b. Since, the parametric studies varying the phasing of the rear fin showed that the rear fin produces the maximum thrust compared to the front fin at  $\delta = -43.6^\circ$ , further studies varying the vehicle speed were performed at this phase. The time history of the thrust produced by the front and rear fins are shown in Fig. 28. At hover, the thrust produced by the front and rear fins are identical and are positive throughout the stroke. As the vehicle speed is increased to 0.25kt, the maximum thrust produced in the midstroke is reduced. Also, the peak thrust produced just after the stroke reversal, due to the wake capture effect, is also reduced. As the vehicle speed is increased further, the thrust produced in the midstroke reduces, and the fin produces a drag around stroke reversal for the front fin, Fig. 28a, and just after stroke reversal, Fig. 28b, for the rear fin. At a vehicle speed of 1kt, the thrust produced by the rear fin exhibits a larger peak after stroke reversal, (black line in Fig. 28b), compared to that of the front fin, Fig. 28a, thus producing a higher mean thrust.

Figure 29a, shows the thrust produced by the front and rear fins, the drag on half the body from steady state computations at  $\alpha = 0^\circ$ , and the total thrust on the vehicle from unsteady computations. From the thrust balance between the total fin thrust and the steady state drag, the vehicle should be able to maintain a forward speed of nearly 0.9kts. The interaction of the flapping fin and the servo boxes with the body produced additional drag on the vehicle. Hence, from the mean thrust of the unsteady simulations it is clear that the vehicle can maintain nearly 0.8kts of forward speed. This forward speed is only slightly higher than our previous two fin vehicle speed of 0.66kts, mainly due to the larger drag on the vehicle. As the vehicle speed is increased from hover to  $V = 1kt$ , the rear fin produces more than double the thrust produced by the front fin, shown in Fig. 29b. The reason for this is due to the stronger wake capture effect after stroke reversals for the rear fin, and the effect of the oncoming flow from the wake of the

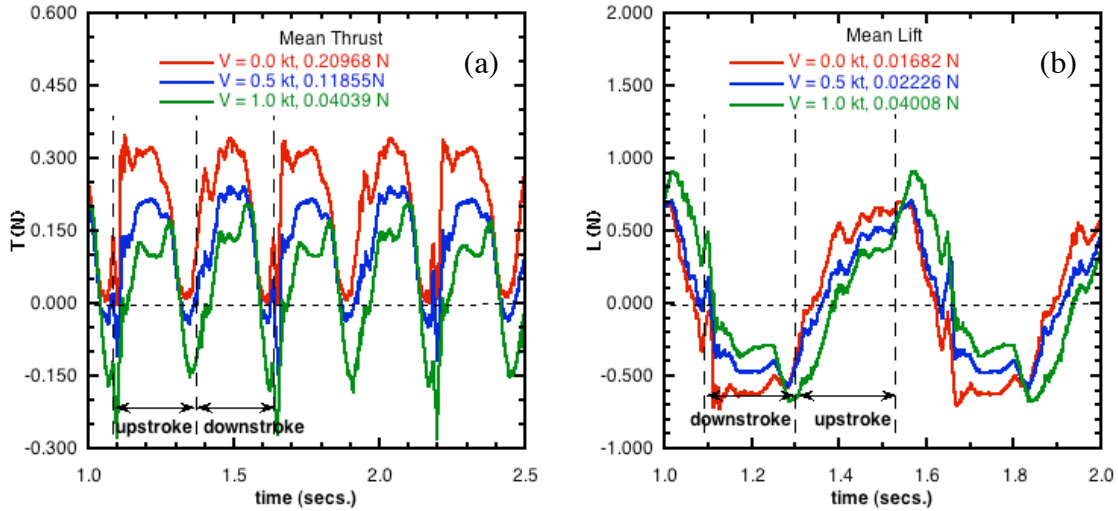


Fig. 27. Effect of inflow velocity on thrust and lift production from a single flapping fin.

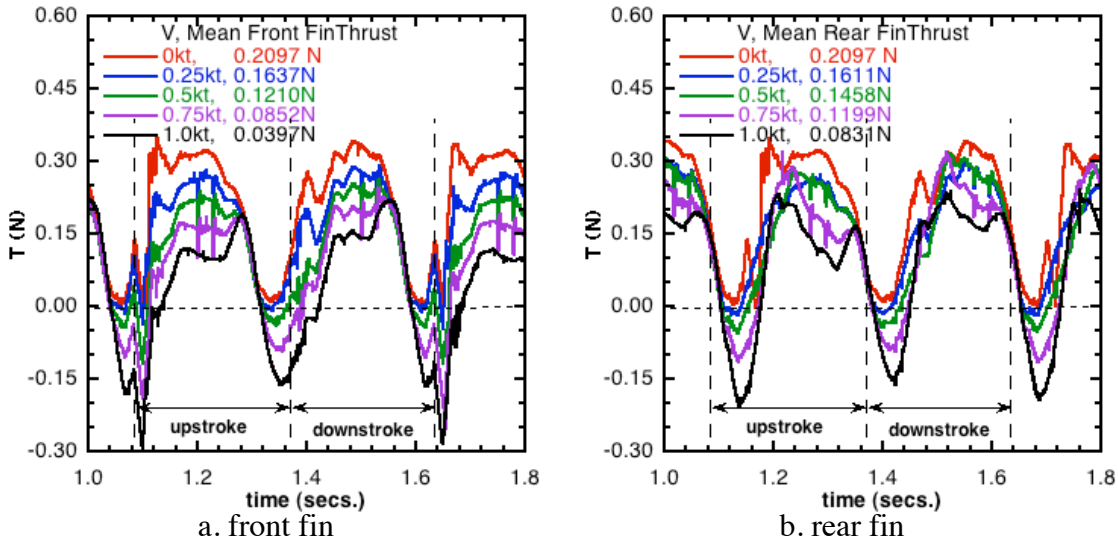


Fig. 28. Variation of unsteady thrust production from the flapping fins with vehicle speed.

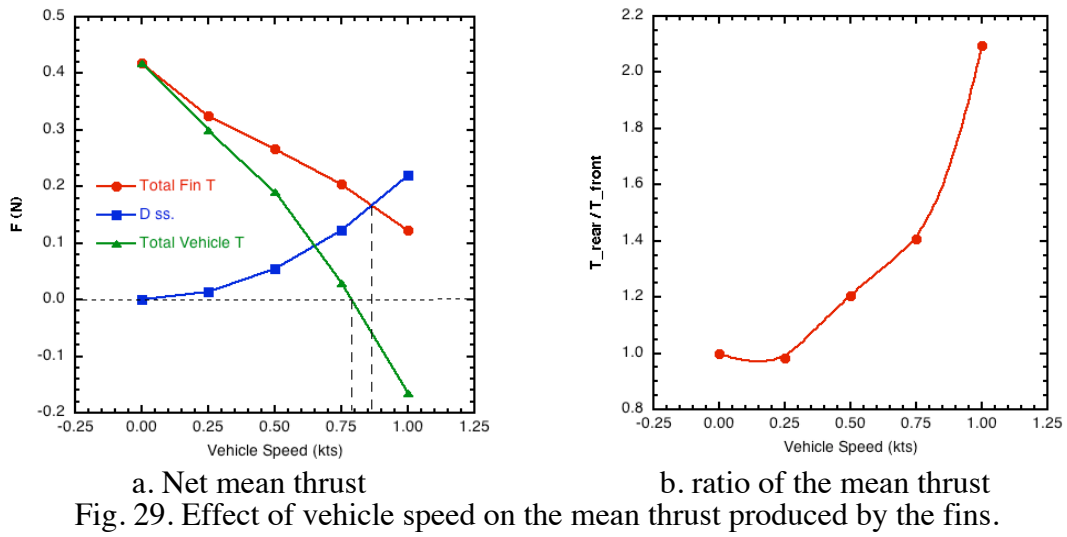
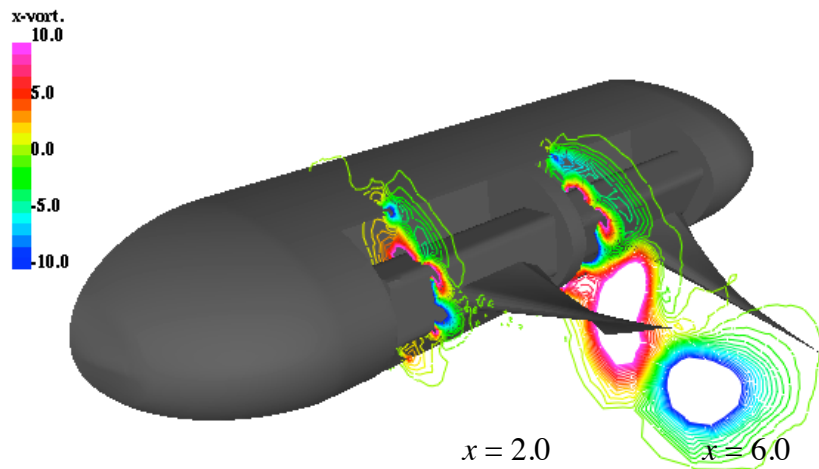
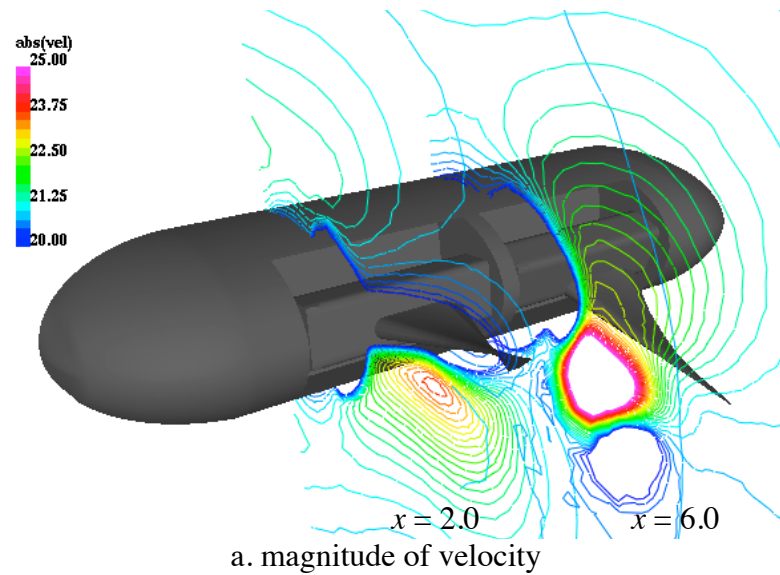


Fig. 29. Effect of vehicle speed on the mean thrust produced by the fins.



b. streamwise component of vorticity

Fig. 30. Inflow conditions for the front and rear fins at  $t = 1.208s$ ,  $V = 1kt$ ,  $\delta = -43.6^\circ$ .

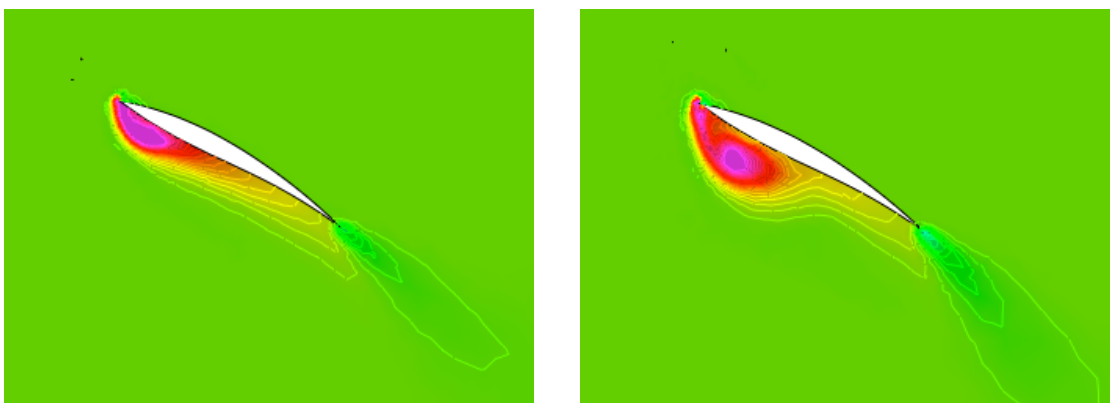


Fig. 31. Spanwise component of vorticity at  $z = 6.5''$ ,  $V = 1kt$ ,  $\delta = -43.6^\circ$ .

front fin. The flow just upstream of the front and the rear fins are very different, as shown in Fig. 30, at two planes,  $x = 2.0$  and  $6.0$ , just ahead of the leading edges of the fins. The magnitude of velocity, Fig. 30a, shows a high velocity region (magenta), in the mid chord of the rear fin and a wake region (blue) towards the wing tip region. This is also clear in the streamwise component of vorticity contours shown in Fig. 30b. Due to these changes in the incoming flow conditions, the wake capture effect of the rear fin is strengthened and leads to the additional thrust. Figure 31 shows the spanwise component of vorticity at  $z = 6.5$ , for the front and rear fins. It is clear that the vortex that is formed on the rear fin is much stronger compared to that on the front fin, leading to a lower pressure on the bottom surface of the rear fin, and thus producing a higher thrust. Figure 32 shows the particle traces released from a horizontal rake just in front of the leading edges of the front and rear fins. This initial time sequence shows the interaction of the leading edge vortex that is shed from the front fin and its interaction with the rear fin. Figure 33 shows the particle traces at the end of 4 flapping cycles, and show that the wing tip and trailing edge vortices are merged. These vortices shed at the beginning of the downstroke are at the top and the ones that were shed at the beginning of the upstroke are seen at the bottom. Also, it is clear that the flow is not dissipated for more than 3 body lengths.

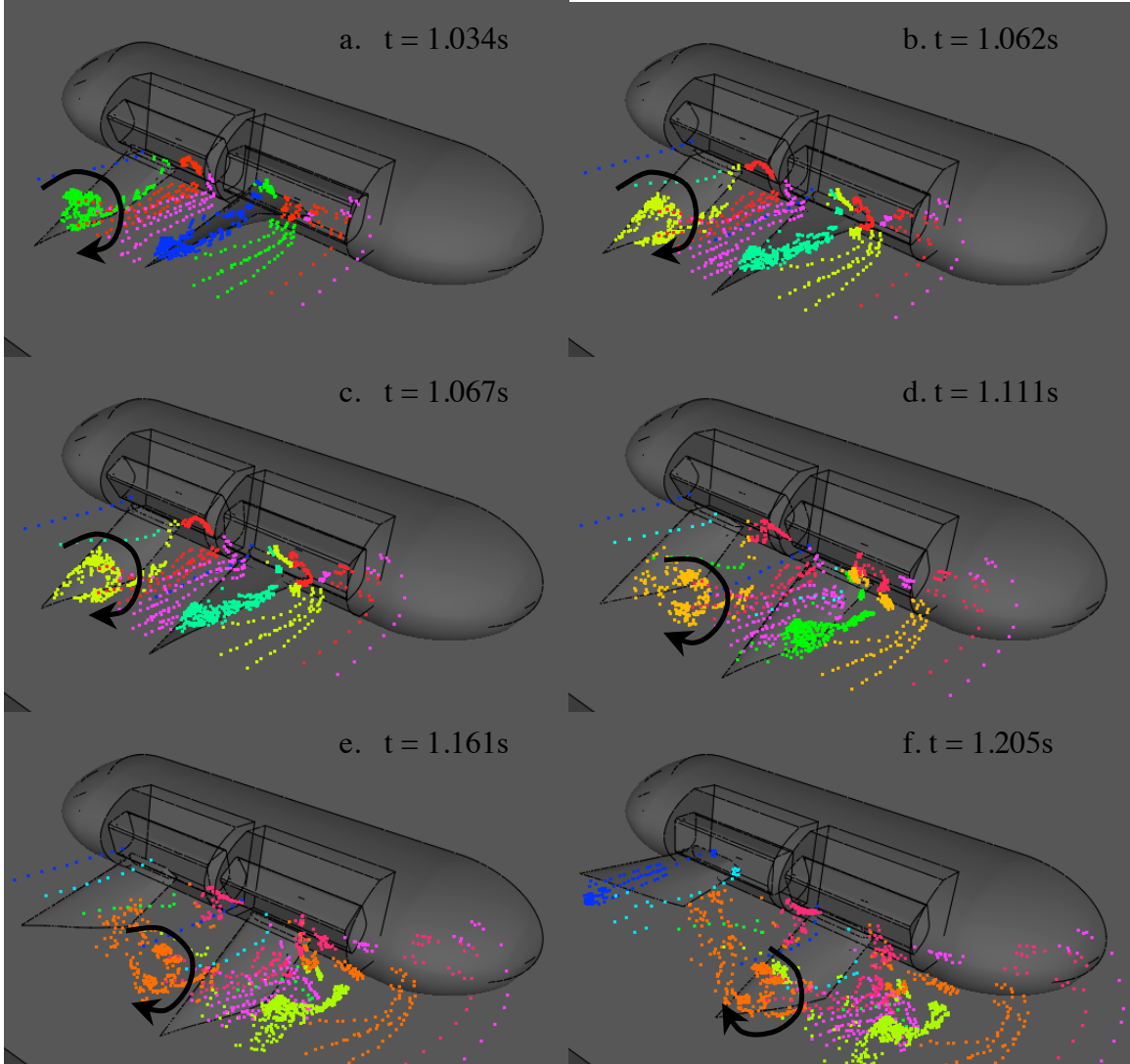


Fig. 32. Particles traces just near stroke reversal of the front and rear fins into upstroke.

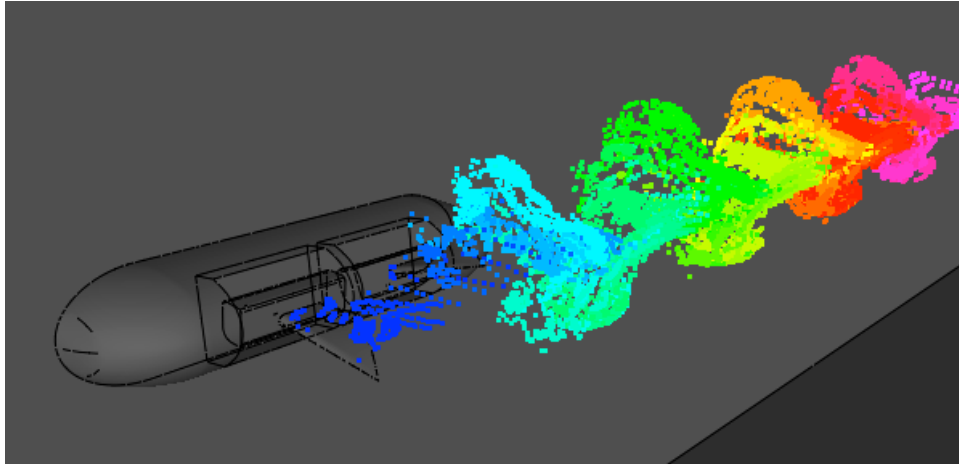


Fig. 33. Particles traces after 4 flapping cycles.

### Vertical Position Control:

In order to effectively control the vertical position of the vehicle, three methods of positive lift production were considered. First, the effect of biasing the stroke amplitude of the rear fin with respect to the front fin is studied. For this, the starting location  $\phi_0$ , of the downstroke of the rear fin is modified from  $45^\circ$  above the horizontal to  $35^\circ$ ,  $25^\circ$  and  $15^\circ$ . The thrust and the lift produced by the rear fin for various biasing angles is shown in Fig. 35. The effect of biasing the rear fin is very minimal on the mean thrust produced by the rear fin which increases from 0.073N to 0.076N, as the biasing is increase by  $30^\circ$ , but the mean lift produced varies from +0.044N to -0.056N, suggesting a viable control parameter for vertical stability of the vehicle.

Another means of producing lift on the vehicle that was tested is to maintain the front fin at an orientation corresponding to  $t = 0.1s$ , Fig. 36 and flapping only the rear fin according to the kinematics in Fig. 16. In this configuration, at  $V = 1kt$ , the front fin produces a mean lift of 0.42N and a drag of 0.19N while the rear fin produces a lift of -0.036N and a thrust of 0.063N, as shown in Fig. 37. The mean total thrust and lift on the vehicle are -0.43N and 0.53N, respectively. At a reduced vehicle speed of 0.5kt, the total thrust produced on the vehicle is nearly zero with the front fin producing a mean drag of 0.048N while the rear fin produces a thrust of 0.135N; the lift produced by the front fin is reduced by a factor of 4 as expected, while the rear fin produces a mean lift of -0.015 N, Fig. 38. The overall thrust and lift on the vehicle are 0.01N and 0.11N, respectively. Although this configuration provides more lift, the additional drag penalty due to the front fin precludes its use for vertical control of the vehicle.

The third method considered for lift production is to employ a set of kinematics that produces lift, called a lift gait. Two sets of kinematics were tested for this purpose. The first set, shown in Fig. 39, has a bulk rotation behavior similar to the forward thrust kinematics, but the amplitude of bulk rotation is reduced to  $27.4^\circ$  while flapping at higher frequency of 4.62Hz. The relative rotation of the trailing edge, rib 5, is nearly constant with respect to the bulk rotation, compared to the forward gait, where the trailing edge lags the leading edge, rib 1, both during up and downstrokes. The thrust and lift generated with this set of kinematics is shown in Fig. 40. Another set of kinematics that produces lift at a lower flapping frequency of 1.4Hz was also tested and is shown in Fig. 41. In this gait, the downstroke is faster than the upstroke and the

relative positions of the ribs are nearly constant throughout the stroke, maintaining a cupped configuration. The mean lift for this set of kinematics is 0.069N and it also produces a mean thrust of 0.06N.

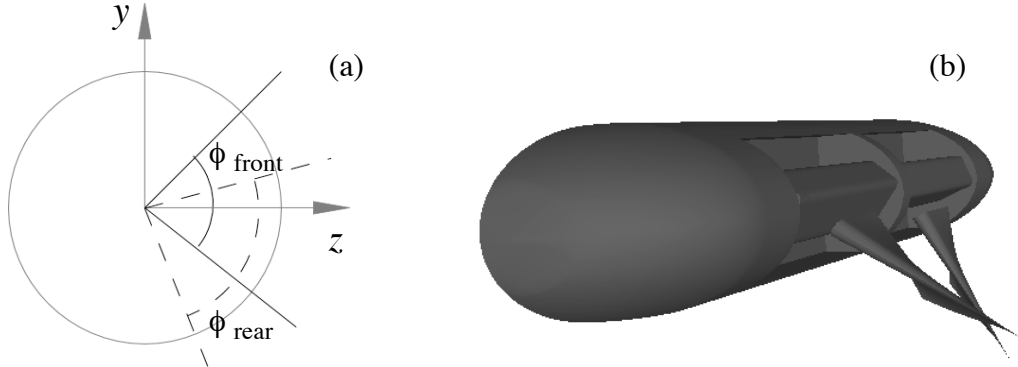


Fig. 34. Biasing of the rear fin, (a) schematic showing the start and end of stroke amplitude (continuous: front fin, dashed: rear fin) and (b) position of the front and rear fins at the beginning of the upstroke.

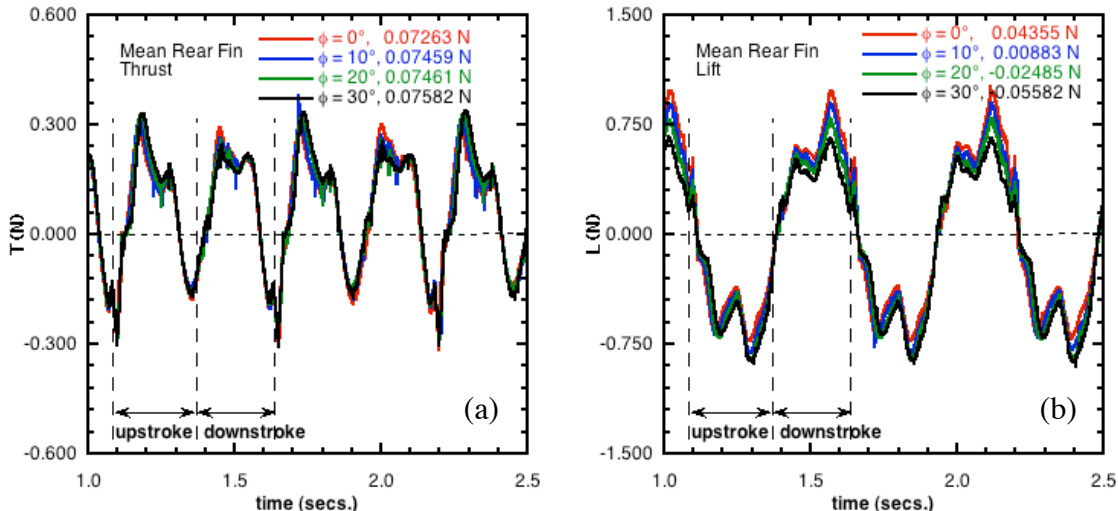


Fig. 35. Thrust and lift variation with rear fin biasing,  $V = 1\text{kt}$ .

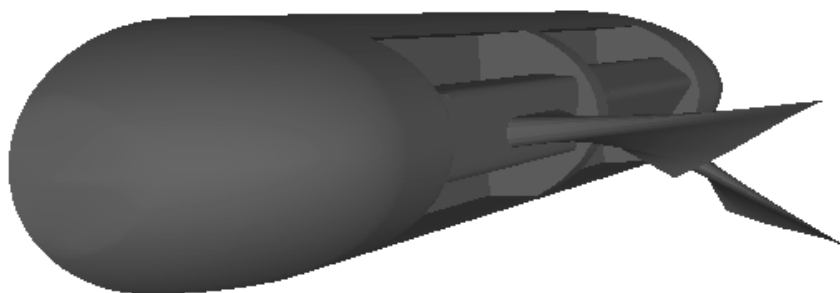
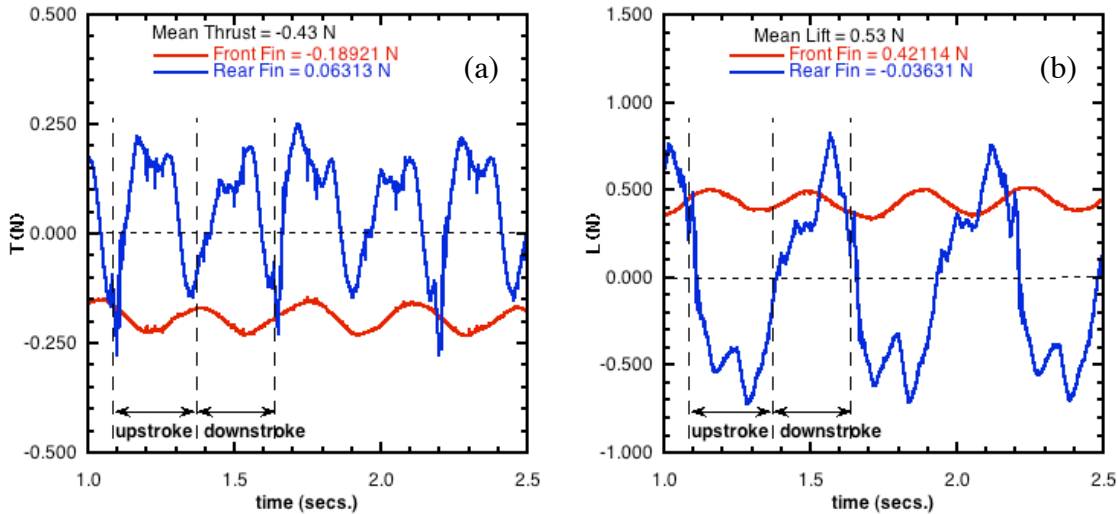
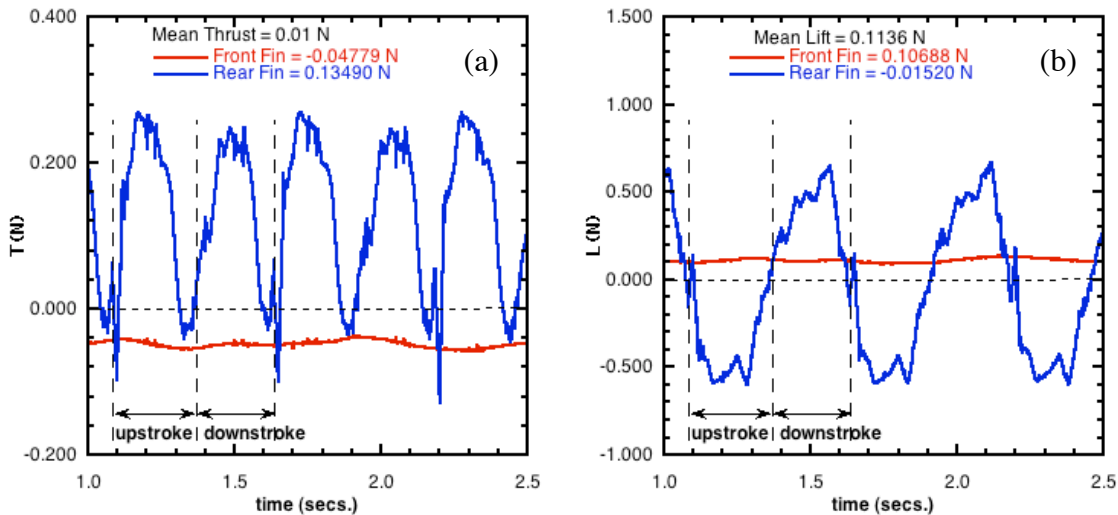
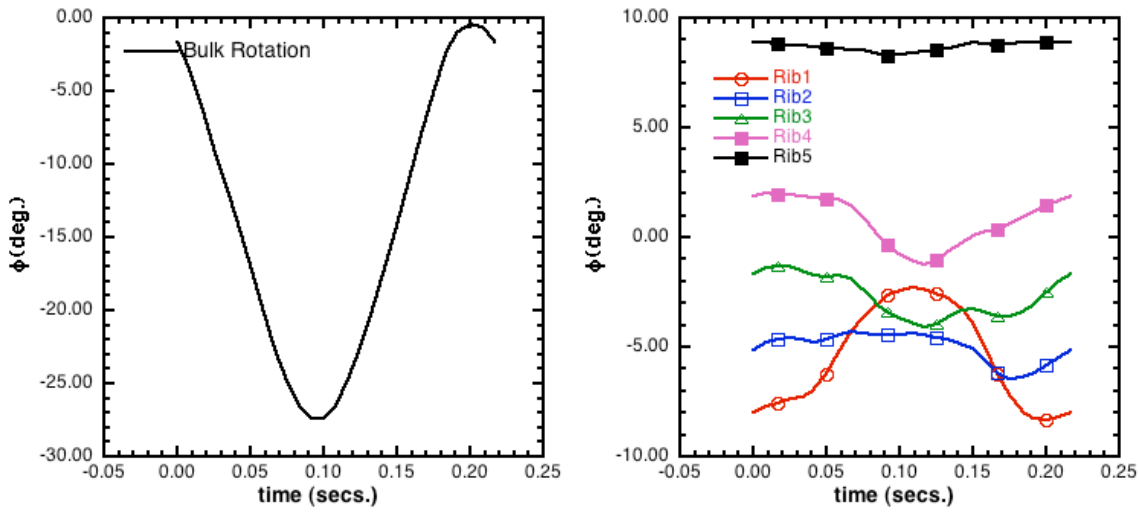


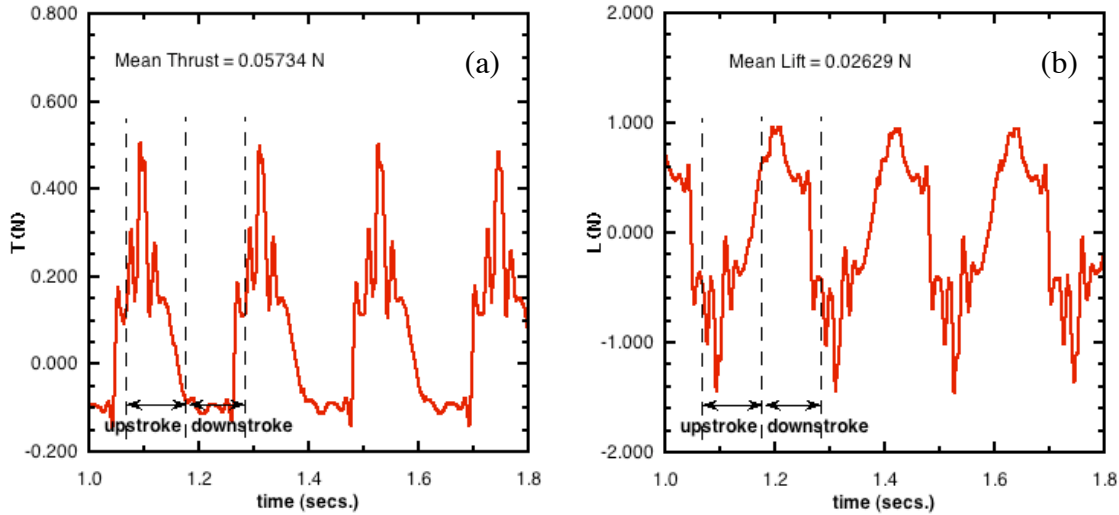
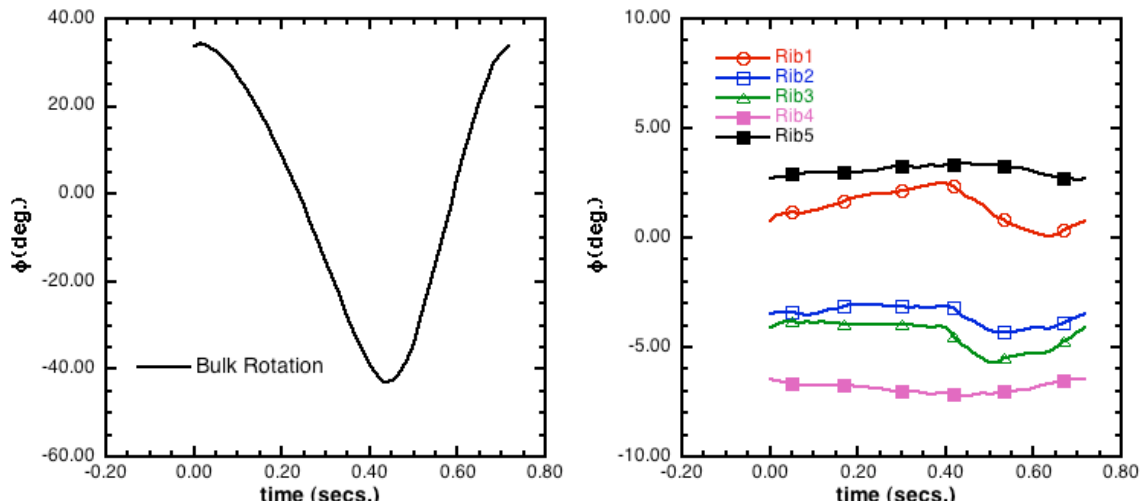
Fig. 36. Configuration of the vehicle with front fin fixed.

Fig. 37. Thrust and lift variation with the front fin fixed,  $V = 1\text{kt}$ .Fig. 38. Thrust and lift variation with the front fin fixed,  $V = 0.5\text{kt}$ .

a. Bulk rotation

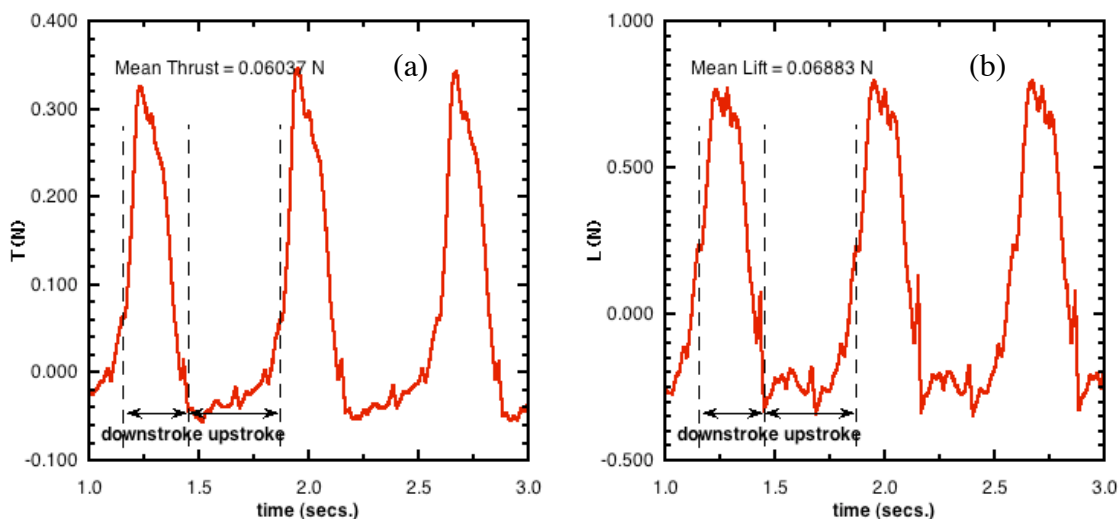
b. Relative rotation

Fig. 39. Kinematics for a flapping deforming fin producing lift,  $f = 4.62\text{Hz}$ .

Fig. 40. Thrust and lift variation with lift kinematics,  $f = 4.62\text{Hz}$ ,  $V = 0\text{kts}$ .

a. Bulk rotation

b. Relative rotation

Fig. 41. Kinematics for a flapping deforming fin producing lift,  $f = 1.4\text{Hz}$ .Fig. 42. Thrust and lift variation with lift kinematics,  $f = 1.4\text{Hz}$ ,  $V = 0\text{kts}$ .

## **Yaw Maneuver:**

In order to simulate a yaw turn of the vehicle, the set of kinematics producing forward thrust, Fig. 16, is used for the left side fins, while a set of kinematics that produces a reverse thrust, Fig. 43, is used for the right side fins scaled to match the frequency of the front fin. This flow past an isolated fin flapping with this set of kinematics was first simulated. The bulk rotation for this set is similar to that of the forward thrust producing kinematics. The relative rotations of the ribs are reversed compared to Fig. 16b, and rib 5 leads rib 1 throughout the flapping cycle. The thrust and lift time histories are shown in Fig. 44. With the fin flapping at 1.765Hz, a mean thrust of nearly  $-0.14\text{N}$  is produced and the mean lift produced is nearly zero. As the mean reverse thrust is smaller compared to the mean forward thrust produced by the kinematics,  $0.21\text{N}$ , the relative rotations of the forward gait, Fig. 16b, were halved. This is based on our previous study, Ramamurti et al [7], on varying the flexibility of the fin past an isolated flapping fin.

For the yaw maneuver simulation, the complete vehicle with four flapping fins was considered, and the net forces and moments were computed. The mesh that was employed for the simulation consists of 1.9M points and 10.7M tetrahedral elements. In this initial simulation the vehicle was held in place with all the 4 fins flapping. The time history of forces and moments produced are shown in Fig. 45. The mean thrust produced by the left and the right fins are -0.41N and 0.34N, respectively, Fig. 45a; the mean total thrust and lift on the vehicle are -0.07N and 0.068N, Figs. 45b and c. The mean side force on the vehicle is nearly 0.02N, Fig. 45d. The mean yaw moment produced by the left and right fins are 0.058N-m and 0.045N-m, respectively, Fig. 45e and the mean total yaw moment on the vehicle is 0.103N-m, Fig. 45f. The mean pitch and the roll moments are nearly zero.

Next, the vehicle was unconstrained in the yaw degree of freedom, while all the other degrees of 6-dof model were constrained. For this simulation, the moment of inertia of the yaw axis of the vehicle though the center of gravity was computed both from the volume representation in the simulations and from the actual vehicle geometry obtained from experiments, and are  $0.0483\text{Kg m}^2$  and  $0.0262\text{Kg m}^2$ , respectively. The total force and moment time history on the maneuvering vehicle using the experimental value is shown in Fig. 46.

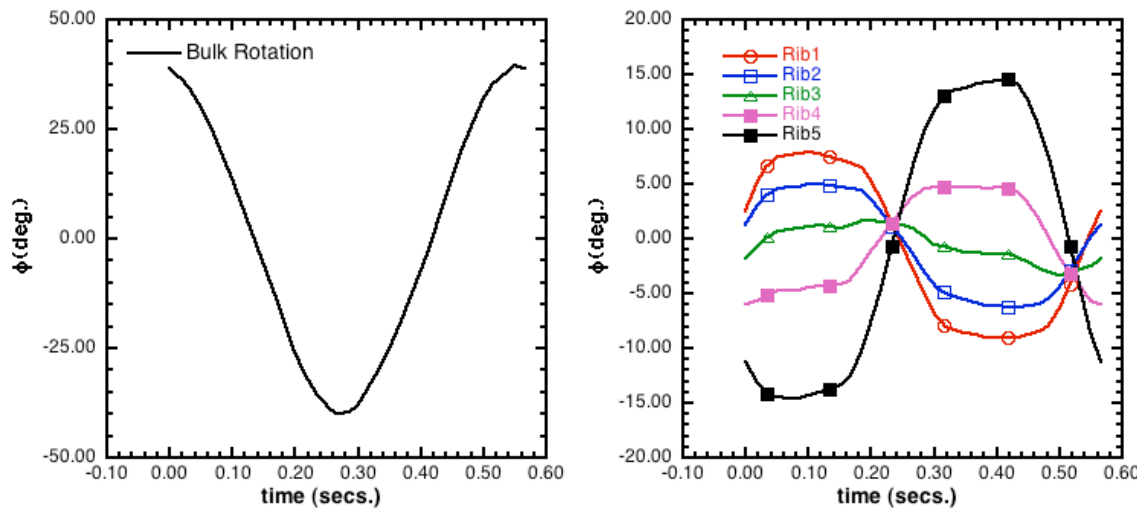


Fig. 43. Kinematics for a flapping deforming fin producing reverse thrust,  $f = 1.765\text{Hz}$ .

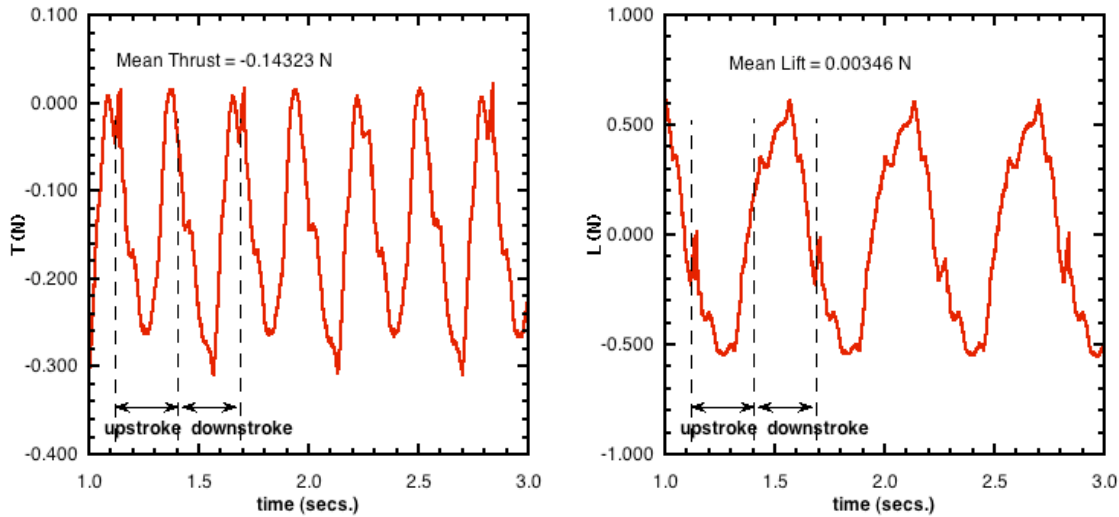
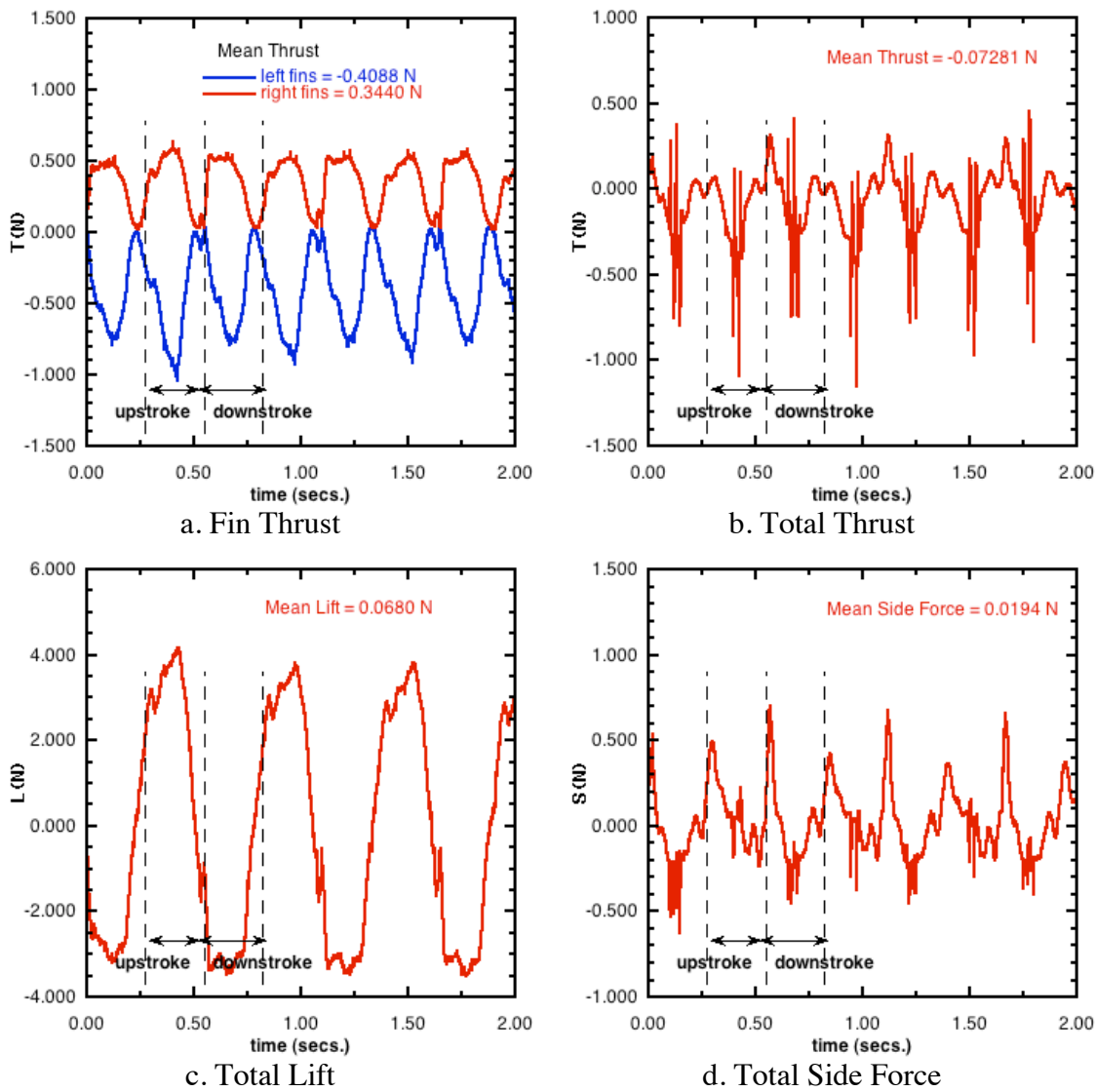


Fig. 44. Thrust and lift variation with reverse thrust kinematics,  $f = 1.765\text{Hz}$ ,  $V = 0\text{kts}$ .



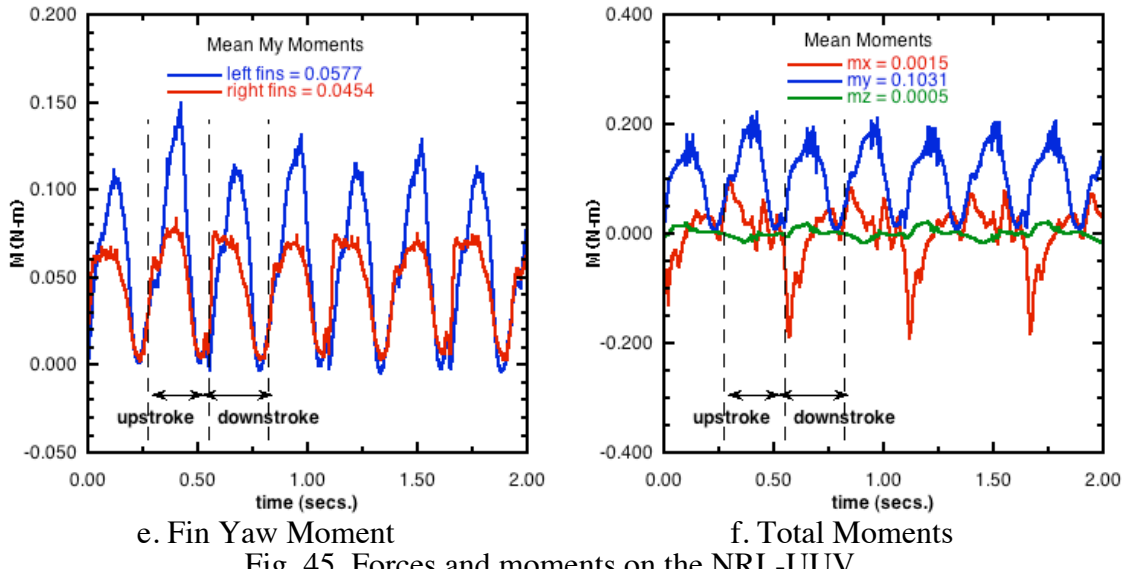


Fig. 45. Forces and moments on the NRL-UUV.

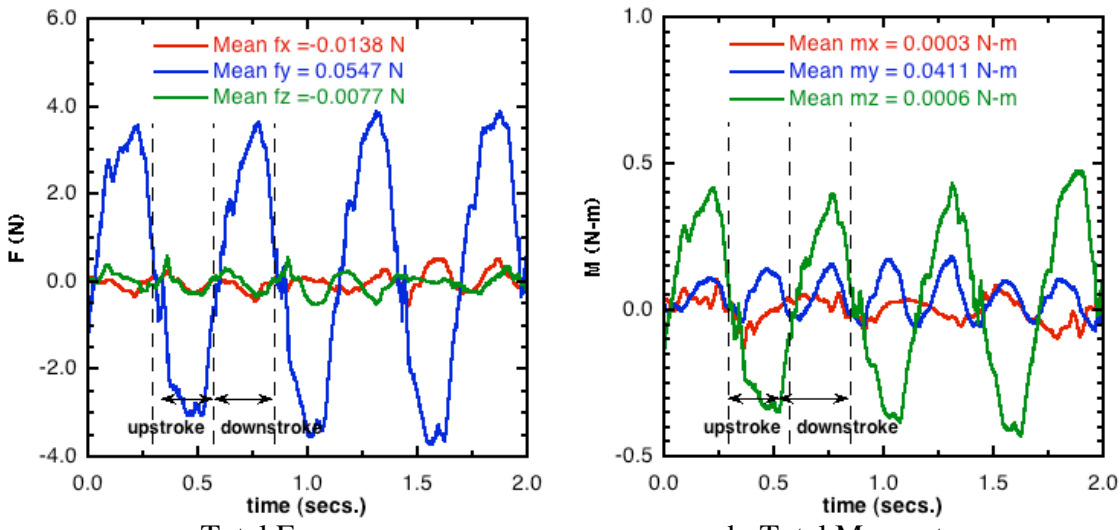


Fig. 46. Forces and moments on the NRL-UUV undergoing a yaw maneuver.

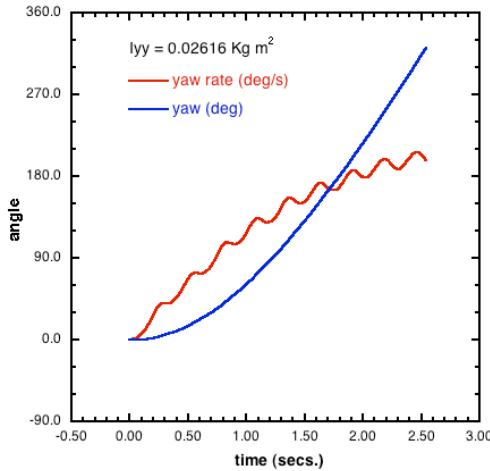
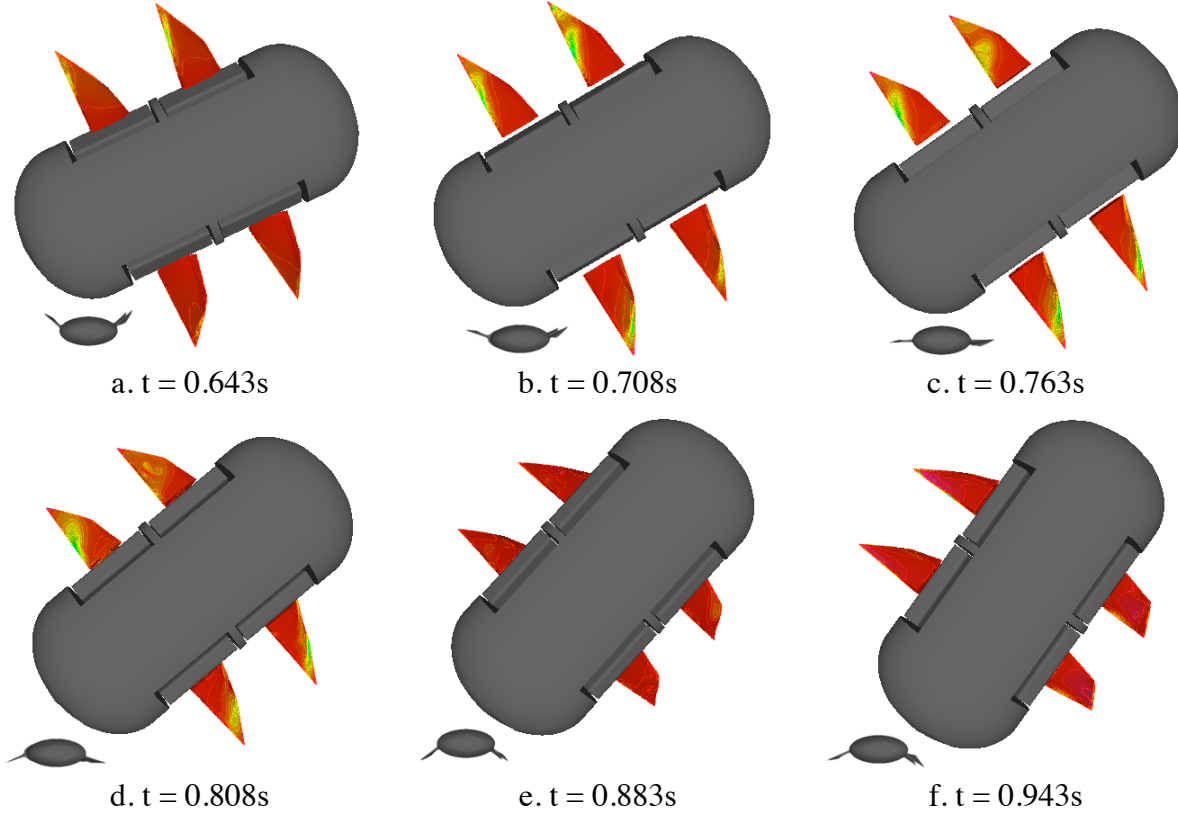


Fig. 47. Trajectory of NRL-UUV during a yaw turn.

The force time history, Fig. 46a, shows that the mean thrust and side forces are nearly zero and that the vertical force exhibits a larger range of variation. The moment time history, Fig. 46b, shows that the yaw moment,  $M_y$ , remains positive for the entire maneuver and the pitch moment despite having a larger range of values has a nearly zero mean moment. The yaw rate and the yaw turn angle of the vehicle are shown in Fig. 47. It is clear that the vehicle completes a full turn in nearly 2.5s. The yaw turn rate shows an oscillatory behavior arising from the total yaw moment on the vehicle and achieves an asymptotic value of nearly  $180^\circ/s$ . This turn rate is higher than that observed in the experiments which has a maximum rate of  $40^\circ/s$ . The differences may be due to the moment of inertia that is used in the simulation which is nearly half that is based on volume and the kinematics that were employed in the simulation are different from that of the experiments. Hence, the experimental kinematics have to be obtained and will be used in the future simulations for comparison. The surface pressure distribution on the flapping fins and their orientation during a cycle during the maneuver is shown in Fig. 48.

The computational effort involved for this unsteady maneuvering simulation is 41K timesteps with several local and global remeshes and spans nearly a week of wall clock time using 32 processors on an SGI Altix 3700. Another simulation was performed by enclosing the maneuvering body inside a box within which the mesh moves rigidly with the body with the exception of a few layers of mesh that surrounds the flapping body. This reduces the computational time and a 3.5s simulation of the maneuver was completed in 36K timesteps, resulting in a speed up of nearly 1.6 in the total computational effort.



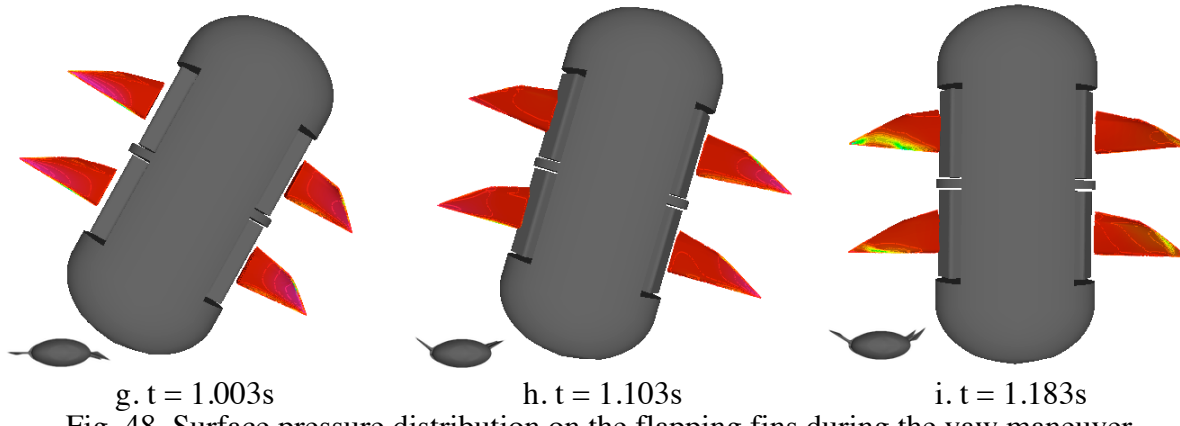


Fig. 48. Surface pressure distribution on the flapping fins during the yaw maneuver.

### Effect of Fin Orientation:

Another method of rapidly make a  $180^\circ$  turn is to make the vehicle symmetric front to back by orienting the rear fins such that the longer leading edge faces the rear of the vehicle, as shown in Fig. 49. In this case, the kinematics for the front and rear fins can be swapped to enable a quick reverse thrust on the vehicle. For these simulations, the fins that are facing the free stream velocity are termed the front fins. First, simulations were performed for this configuration with the front fins using the forward thrust gait, Fig. 16, and the rear fins using a reverse thrust gait, Fig. 43. Figure 50 shows the thrust and lift generated in this configuration at a vehicle speed of 1kt. It is clear that the rear fin produces nearly 5 times the thrust of the front fin, compared to nearly twice when the rear fin is oriented forward and using the forward thrust kinematics. The total drag on the vehicle is 0.087N. The lift produced by the rear fin is reduced to nearly zero compared to 0.045N, Fig. 22b. As the vehicle speed is decreased to 0.5kt, the total thrust on the vehicle is 0.244N, Fig. 51a, and the rear fin produces nearly 1.6 times the thrust from the front fin, compared to 1.2 times in the original configuration, Figs. 28 and 29b. In this configuration the vehicle will be able to maintain a forward speed of 0.88kts. The reason for the increased thrust from the rear fin is mainly due to the selected kinematics and the orientation of the rear fin in the oncoming wake of the front fin as shown in Fig. 52. High pressure region extends on most of the top surface of the rear fin, Fig. 52d, while the fin is tilted forwards. At this instant, although the front fin has a similar orientation, Fig. 52a, the surface pressure on the top surface, Fig. 52b, is much reduced.

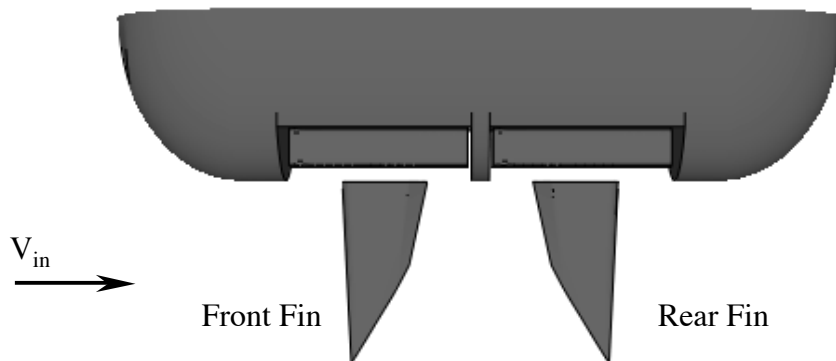


Fig. 49. Vehicle configuration with symmetric fin orientation.

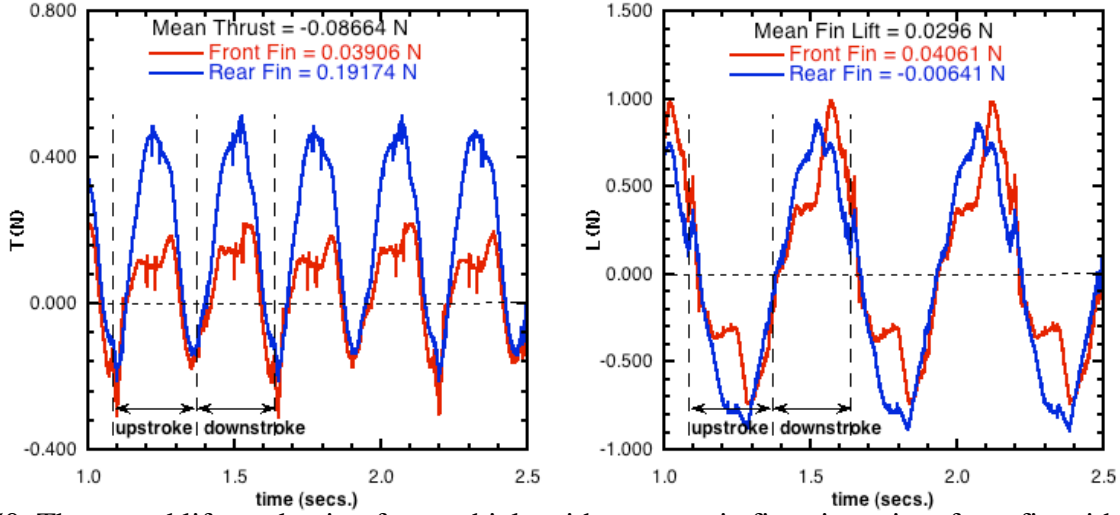


Fig. 50. Thrust and lift production for a vehicle with symmetric fin orientation, front fin with forward thrust kinematics and rear fin with reverse thrust kinematics,  $V = 1\text{kt}$ .

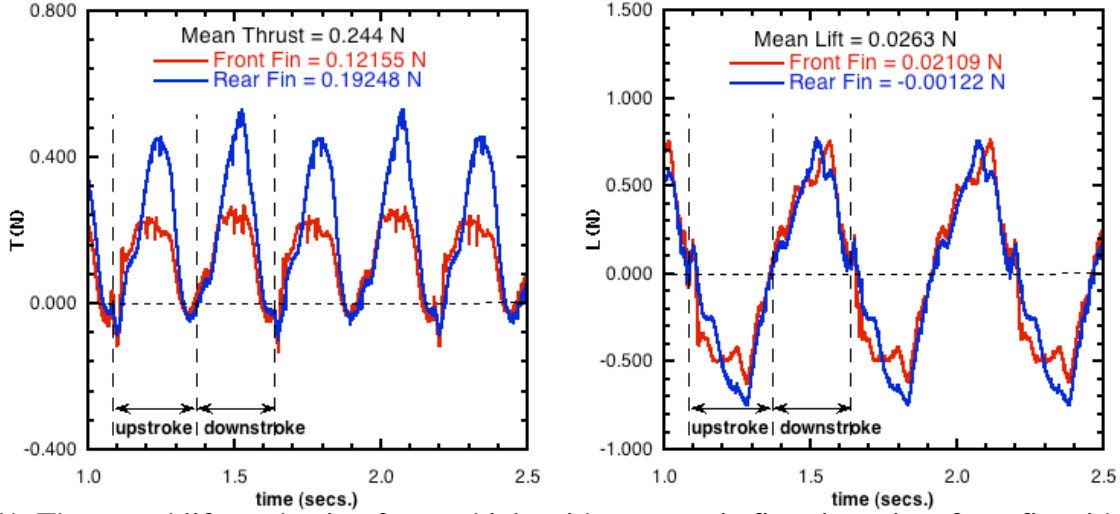


Fig. 51. Thrust and lift production for a vehicle with symmetric fin orientation, front fin with forward thrust kinematics and rear fin with reverse thrust kinematics,  $V = 0.5\text{kt}$ .

All possible combinations of kinematics for the front and the rear fins with forward and reverse thrust kinematics were simulated at both 0.5kts and 1kt vehicle speed. In terms of reverse thrust, the combination of using forward thrust kinematics for the front and rear fins, produced a reverse thrust of nearly 0.77N at 1kt vehicle speed; the combination of reverse thrust for the front fin and forward thrust for the rear fin produced 0.67N of reverse thrust. At a lower vehicle speed of 0.5kt, the latter combination produces slightly more reverse thrust of 0.38N compared to the former combination of 0.3N. Hence, the latter combination using reverse thrust for the front fin and forward thrust for the rear fin can be used to quickly brake the vehicle and reverse to avoid obstacles. Yaw and dive maneuvering simulations are conducted using the experimental kinematics with the symmetric fin orientation.

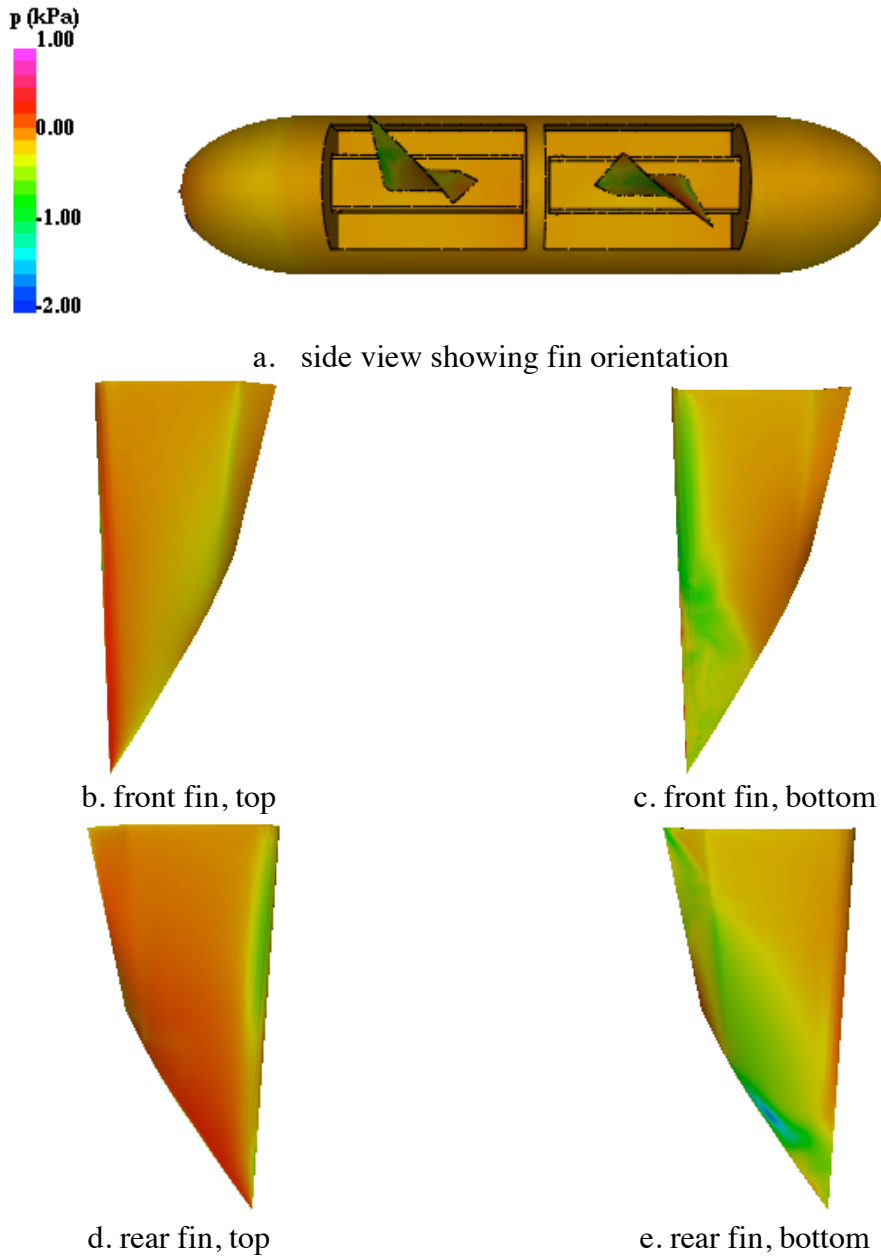


Fig. 52. Surface pressure distribution on vehicle with symmetric fin orientation,  $t = 1.215s$ ,  $V = 1kt$ .

#### Yaw Maneuver using Symmetric Fin Orientation:

A yaw maneuver in this configuration uses the combination of forward thrust for the front fin and reverse thrust for the rear fin on the right side of the vehicle and the anti-symmetric combination on the left side of the vehicle. Simulations were performed using moments of inertia based on both the volume and the experimental values. The mean yaw moment during a 3sec maneuver starting from rest is nearly 0.027 N-m compared to 0.0411 N-m for the vehicle with both fins oriented forward. Figure 53 shows the yaw rate for this configuration asymptotes to nearly  $160^\circ/s$ . As the moment of inertia is increased to the value based on volume the yaw rate drops to  $140^\circ/s$ . The mean yaw moment for this case is 0.035 N-m.

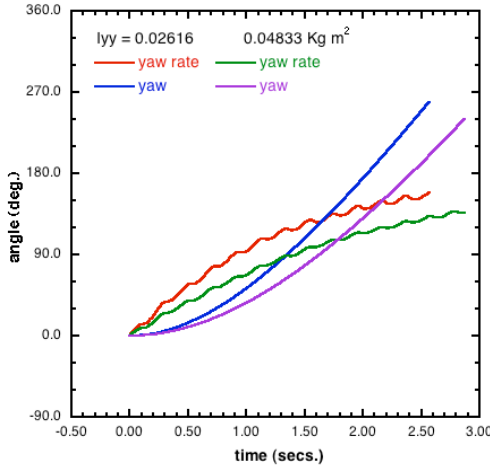
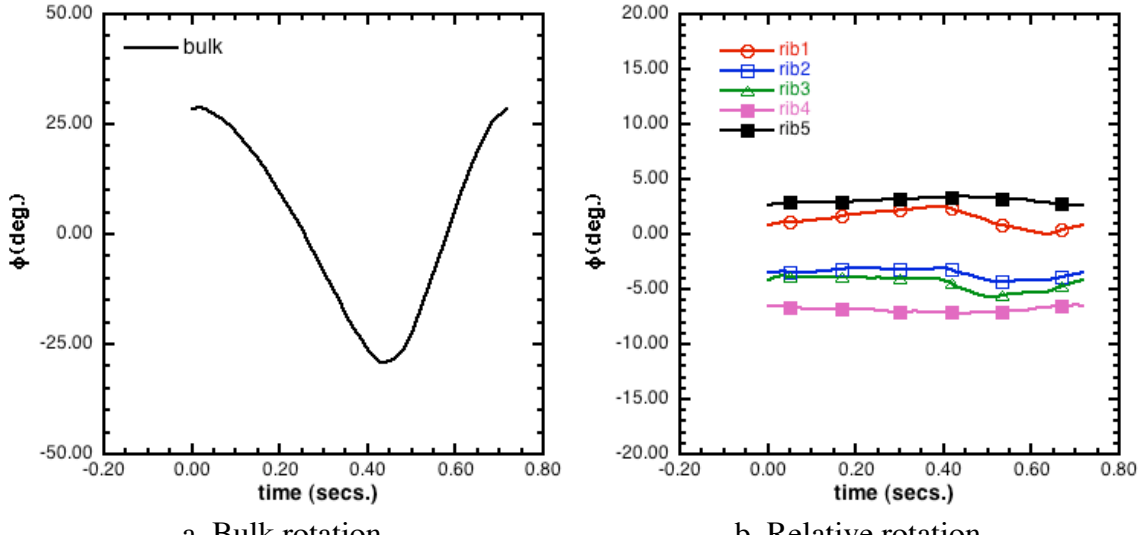


Fig. 53. Effect of moment of inertia on the yaw turn for NRL-UUV with symmetric fin orientation.

#### Dive Maneuver using Symmetric Fin Configuration:

Using the symmetric configuration of the fins and kinematics corresponding to negative lift, a vertical maneuver of the vehicle is simulated. The kinematics that produces the negative lift is shown in Fig. 54. The fin has a cupped shape throughout the entire cycle, fig. 54b, with a slightly faster upstroke compared to the downstroke, Fig. 54a. The time history of thrust and lift using this negative lift gait on isolated flapping fin is shown in Fig. 55. This fin produces a mean lift of -0.058 N and a forward thrust of 0.035N when flapping at 1.4Hz. The vehicle mass is assumed to be 2.9Kg which is obtained from the experiments. Figure 56 shows the results of the simulations over 5 flapping cycles. The velocity of the vehicle undergoes an oscillatory behavior due to the flapping cycle of the fin and the vehicle descends at the rate of 4.5cm/sec consistent to the results observed in the experiment.



a. Bulk rotation  
b. Relative rotation  
Fig. 54. Kinematics for a flapping deforming fin producing negative lift,  $f = 1.395\text{Hz}$ .

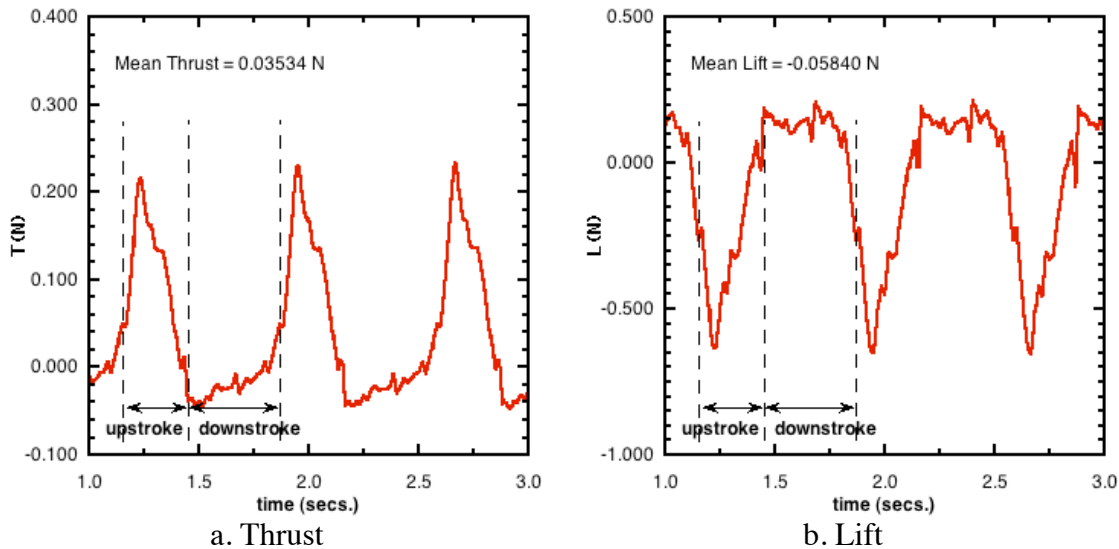


Fig. 55. Thrust and lift variation with cupped kinematics,  $f = 1.395\text{Hz}$ ,  $V = 0\text{kts}$ .

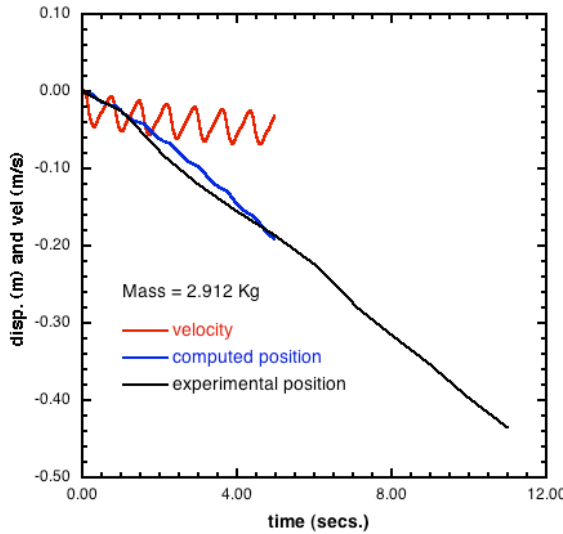


Fig. 56. Trajectory of the NRL-UUV during a dive maneuver,  $f = 1.395\text{Hz}$ .

## SUMMARY

The 3-D unsteady computations past a UUV with four actively controlled curvature fins were carried out. Several cross sections of the vehicle were considered and based on the minimum drag an elliptical cross section was chosen. Hydrodynamic characteristics of the vehicle for various angles of attack, side slip angles, and turn characteristics were simulated and were incorporated in the dynamic modeling of the vehicle. Parametric studies varying the spacing between the front and rear fins showed that the wake capture effect was not pronounced at hover, but is significant as the vehicle speed increased. At a vehicle speed of 1kt, the rear fins produce nearly 1.8 times the thrust as that of the front fins, and improve further to a factor of 2.1 when they are lagged in phase by nearly  $44^\circ$ . The mean thrust from the unsteady simulations showed that the vehicle was able to maintain a forward speed of nearly 0.8kts. Several methods of vertical position control were studied and the stroke angle biasing provided a viable method. The thrust and lift production for various gaits producing forward thrust, reverse thrust and lift

were computed and used for the development of the controller for the vehicle. The unsteady flow solver with flapping deforming fins was coupled to a 6-dof trajectory model and was tested to simulate a yaw turn. For this maneuver, the right side of the fins used a forward thrust producing gait with reduced flexibility and the left side fins used a reverse thrust producing gait, resulting in a yaw turn. The results showed that the vehicle turning rate was nearly 180°/s. The effect of fin orientation was studied by making the vehicle symmetric front to back and using various combinations of forward and reverse thrust producing kinematics. It was found that using forward thrust kinematics for the front fin and reverse thrust kinematics for the rear fin produced enough thrust to maintain a velocity of nearly 0.9kts. Good agreement is obtained between the experimental and computed trajectories for a dive maneuver.

## ACKNOWLEDGEMENTS

This work was supported by ONR through an NRL 6.2 project: "Unsteady Hydrodynamics of Swimming Vehicles." The valuable discussions with Dr. B.R. Ratna, Dr. W.C. Sandberg, J. Palmisano, M. Preussner, and Prof. Rainald Löhner of George Mason University are greatly appreciated. This work was supported in part by a grant of HPC time from the DoD HPC center for the NRL SGI-Altix.

## REFERENCES

1. Blake R.W., "The mechanics of labriform motion I. Labriform locomotion in the angelfish (*pterophyllum eimekei*): An analysis of the power stroke", *J. Exp. Biol.*, **82**, 1979, pp. 255-271.
2. Kato, N., Liu, H. and Morikawa, H., "Biology-Inspired Precision Maneuvering of Underwater Vehicles," *Proc. of the 12<sup>th</sup> Intl. offshore and Polar Engg. Conf.*, Vol. 2, 2002, pp. 269-276.
3. Ando, Y., Kato, N., Suzuki, H., Ariyoshi, T., Suzumori, K., Kanda, T. and Endo, S., "Elastic Pectoral Fin Actuators for Biomimetic Underwater Vehicles," *Proc. of the 16<sup>th</sup> Intl. offshore and Polar Engg. Conf.*, 2006, pp. 260-267.
4. Tangorra, J.L., Davidson, S. N., Hunter, I., Madden, P.G.A., Lauder, G.V., Dong, H., Bozukurttas, M. and Mittal, R., "The Development of a Biologically Inspired Propulsor for Unmanned Underwater Vehicles," *IEEE J. of Ocean Engg.*, Vol. 32, No. 3, July 2007, pp. 533-550.
5. Ramamurti, R. and Sandberg, W.C., "A 3-D Computational Study of the Aerodynamic Characteristics of Insect Flight," *J. exp. Biology*, Vol. 205, No. 10, pp. 1507-1518, May 2002.
6. Ramamurti, R., Sandberg, W.C., Löhner, R., Walker, J.A. and Westneat, M.M., "Fluid Dynamics of Flapping Aquatic Flight in the Bird Wrasse: 3-D Unsteady Computations with Fin Deformation," *J. exp. Biology*, Vol. 205, No. 19, pp. 2997-3008, October 2002.

7. Ramamurti, R., Geder, J.D., Palmisano, J., Ratna, B. and Sandberg, W.C., "Computations of Flapping Flow Propulsion for Unmanned Underwater Vehicle Design," *AIAA J.*, Vol. 48, No. 1, pp. 188-201, January 2010.
8. Palmisano, J., Ramamurti, R., Lu, K.J., Cohen, J., Sandberg, W. C. and Ratna, B., "Design of a Biomimetic Controlled-Curvature Robotic Pectoral Fin," *2007 IEEE Int. Conf. on Robotics and Automation*, Roma, Italy.
9. Geder, J., Ramamurti, R., Palmisano, J., Pruessner, M., Ratna, B. and Sandberg, W. C., "Sensor Data Fusion and Submerged Test Results of a Pectoral Fin Propelled UUV," *16th International Symposium on Unmanned Untethered Submersible Technology*, Durham, New Hampshire, USA, August 23-26, 2009.
10. Licht, S., Polidoro, V., Flores, M. and Hover, F.S., "Design and Projected Performance of a Flapping Foil AUV," *IEEE J. of Ocean Engg.*, Vol. 29, No. 3, July 2004.
11. Dickinson, M. H., Lehmann, F.-O. and Sane, S. P., "Wing rotation and the aerodynamic basis of insect flight," *Science*, Vol. 284, 1999, pp. 1954-1960.

